AGU ADVANCING EARTH AND SPACE SCIENCE

Space Weather

RESEARCH ARTICLE
10.1029/2022SW003308

Key Points:

- Thermosphere Ionosphere Electrodynamics General Circulation Model driven by data-assimilated aurora and electric field better resolves the I-T system responses to the 2015 St. Patrick's Day storm
- Strong neutral upward winds are induced by the enhancement of aurora and electric field, which increases local Joule heating in E-region
- Realistic storm-time I-T responses should have larger dynamic range, richer scales, and stronger variability than default model simulations

Supporting Information:

Supporting Information may be found in the online version of this article.

Correspondence to:

X. Lu,
xianl@clemson.edu

Citation:

Lu, X., Wu, H., Kaeppler, S., Meriwether, J., Nishimura, Y., Wang, W., et al. (2023). Understanding strong neutral vertical winds and ionospheric responses to the 2015 St. Patrick's Day storm using TIEGCM driven by data-assimilated aurora and electric fields. *Space Weather*, *21*, e2022SW003308. https://doi.org/10.1029/2022SW003308

Received 29 SEP 2022
Accepted 11 JAN 2023

Author Contributions:

Conceptualization: Xian Lu
Formal analysis: Xian Lu
Funding acquisition: Xian Lu
Investigation: Xian Lu, Haonan Wu
Methodology: Xian Lu
Project Administration: Xian Lu
Resources: Xian Lu
Supervision: Xian Lu

Understanding Strong Neutral Vertical Winds and Ionospheric Responses to the 2015 St. Patrick's Day Storm Using TIEGCM Driven by Data-Assimilated Aurora and Electric Fields

Xian Lu[1], Haonan Wu[1], Stephen Kaeppler[1], John Meriwether[1], Yukitoshi Nishimura[2], Wenbin Wang[3], Jintai Li[4], and Xueling Shi[3,5]

[1]Department of Physics and Astronomy, Clemson University, Clemson, SC, USA, [2]Department of Electrical and Computer Engineering and Center for Space Physics, Boston University, Boston, MA, USA, [3]High Altitude Observatory, National Center for Atmospheric Research, Boulder, CO, USA, [4]University of Alaska Fairbanks, Fairbanks, AK, USA, [5]Department of Electrical and Computer Engineering, Virginia Tech, Blacksburg, VA, USA

Abstract As one of the strongest geomagnetic storms in Solar Cycle 24, the 2015 St. Patrick's Day storm has attracted significant attention. We revisit this event by taking advantage of simultaneous observations of high-latitude forcings (aurora and electric fields) and ionosphere-thermosphere (I-T) responses. The forcing terms are assimilated to drive the Thermosphere Ionosphere Electrodynamics General Circulation Model (TIEGCM) using a newly adopted Lattice Kriging method (Wu & Lu, 2022, https://doi.org/10.1029/2021SW002880; Wu et al., 2022, https://doi.org/10.1029/2022SW003146). Compared to the default run, the TIEGCM simulation with assimilation captures: (a) secondary E-region electron density peak due to aurora intensification; (b) strongly elevated ion temperatures (up to ~3000 K) accompanied by a strong northward electric field (~80 mV/m) and associated ion frictional heating; (c) elevation of electron temperatures; and (d) substantially enhanced neutral vertical winds (order of 50 m/s). Root-mean-square errors decrease by 30%–50%. The strong neutral upwelling is caused by large Joule heating down to ~120 km resulting from enhanced aurora and electric field. Data assimilation increases the height-integrated Joule heating at Poker Flat to a level of 50–100 mW/m^2 while globally, its maximum value is comparable with the default run: the location of energy deposition becomes guided by data. Traveling atmospheric disturbances in the assimilation run show stronger magnitudes and larger extension leading to an increase of vertical wind variability by a factor of ~1.5–3. Our work demonstrates that data assimilation of model drivers helps produce realistic storm-time I-T responses, which show richer dynamic range, scales, and variability than what has been simulated before.

Plain Language Summary Originated from activity of the Sun, space weather can be notoriously hazardous to space security and infrastructure on the ground. An accurate prediction of space environment during storm time is important to mitigate such impacts and enhance space situation awareness. A long-lasting problem for space weather modeling using Ionosphere-Thermosphere (I-T) models is the lack of realistic forcing as a driver, which often causes an underestimation of storm impacts, especially locally. To conquer this difficulty, our work adopts and extends a data assimilation technique which has been used for lower-atmosphere studies to assimilate aurora and electric fields. The I-T model simulation driven by data assimilation captures realistic dynamics and electrodynamics with model results closer to observations than the one driven by empirical forcings (default run). The more realistic model simulation illustrates that space weather impacts are more dynamic, cause stronger disturbances, and show multi-scale features, compared to previous understandings.

1. Introduction

Joule heating and particle heating induced by particle precipitation are the two most important thermospheric heating sources in the auroral zones and compete with the solar irradiance during geomagnetic storm times (D. J. Knipp et al., 2004). Most of the energy deposited in the magnetosphere by the solar wind is ultimately dissipated in the ionosphere-thermosphere (I-T) system as a result of the convergence of Poynting flux and auroral particle precipitation that heats the atmosphere directly through collision and indirectly by increasing Joule heating (G. Lu et al., 1998; Richmond & Thayer, 2000; Thayer & Semeter, 2004; Thayer et al., 1995). During periods of

Validation: Xian Lu, Haonan Wu, Stephen Kaeppler, John Meriwether, Yukitoshi Nishimura, Wenbin Wang, Xueling Shi
Visualization: Xian Lu
Writing – original draft: Xian Lu
Writing – review & editing: Xian Lu, Haonan Wu, Stephen Kaeppler, John Meriwether, Yukitoshi Nishimura, Wenbin Wang, Jintai Li, Xueling Shi

geomagnetic activity, both auroral precipitation and electric fields are elevated leading to large energy deposition in the I-T region and strong localized Poynting fluxes (e.g., Deng et al., 2011; Fuller-Rowell et al., 1987; Heppner et al., 1993; Wang et al., 2005). For instance, the Defense Meteorological Satellite Program (DMSP) observed a local Poynting flux exceeding 170 mW/m^2 associated with merging at the magnetopause flank and lobe during an east-west interplanetary magnetic field (IMF) dominant event (D. Knipp et al., 2011). Satellite observations have also revealed that localized Earth-directed Poynting fluxes can be several times larger than the prediction from statistical models (order of 15 mW/m^2) during magnetic storms (C. Y. Huang & Burke, 2004; Y. Huang et al., 2016).

Such localized energy deposition and its effects, however, are difficult to capture in I-T models driven by empirical high-latitude inputs obtained from statistical auroral (e.g., Hardy et al., 1985; Newell et al., 2009) and electric field models (e.g., Heelis et al., 1982; Roble & Ridley, 1987; Weimer, 2005). Empirical models usually provide the large-scale (>1,000 km) morphology of the auroral oval, which differs from the auroral precipitation seen in the observations, such as that observed by Time History of Events and Macroscale Interactions during Substorms (THEMIS) ground-based all-sky imagers (ASIs). THEMIS ASIs generally depict rich mesoscale (10s–100s km) structures, while narrow field-of-view imaging reveals even small-scale auroral (<10 km) patterns (Nishimura & Lyons, 2021; Nishimura, Deng, et al., 2021; Nishimura, Verkhoglyadova, et al., 2021). Electric fields in the polar cap and auroral region also exhibit cross-scale spectra ranging from planetary scales down to a few kilometers (Golovchanskaya & Kozelov, 2010; Kozelov & Golovchanskaya, 2006), which deviate from the global large-scale two-cell ion convection pattern (Cousins & Shepherd, 2012a, 2012b). Cousins et al. (2013) performed a scale analysis of electric fields using the Super Dual Auroral Radar Network radars (SuperDARN) and showed that the first several empirical orthogonal function (EOF) modes contribute to global-scale features, while higher order EOFs (>8) contribute to mesoscales (<1,000 km) which have a shorter decorrelation time indicating more variability. Small-scale electric fields have been often observed and found to impact the energy budget during magnetic storms (Codrescu et al., 1995; Cosgrove & Codrescu, 2009). Wu et al. (2020) found that an implementation of electric fields varying on short temporal scales and auroras observed by satellites into the Thermosphere Ionosphere Electrodynamics General Circulation Model (TIEGCM) is essential to reproduce the Thermospheric Temperature Enhancement and Inversion Layer (TTEIL) observed by the Fe-Boltzmann lidar at McMurdo, Antarctica. Sheng et al. (2020) found that the Global Ionosphere Thermosphere Model driven by the THEMIS/ASI auroral observations better resolves the magnitude of traveling ionospheric disturbances (doubled) than that by empirical auroral inputs. Both studies require the fusion of aurora and electric field observations to constrain the model drivers for a better understanding of storm-time I-T responses.

The St. Patrick's Day storm (17 March 2015) is the strongest geomagnetic storm during Solar Cycle 24. A special section in the Journal of Geophysical Research Space Physics entitled "Geospace system responses to the St. Patrick's Day storms in 2013 and 2015" has highlighted a series of storm impacts (S.-R. Zhang et al., 2017 and references therein), ranging from ionospheric tongue of ionization and storm enhanced density at high latitudes, subauroral polarization stream and ion upflow at subauroral and midlatitude regions, to significant Prompt Penetration Electric Field and Disturbance Dynamo Electric Field effects on low-latitude electrodynamics. Neutral dynamics involves composition changes (mainly O/N_2) and the resultant Total Electron Content (TEC) depletion during the storm's recovery phase. The studies that cover both magnetospheric forcings and I-T responses and use well-constrained model to connect them, however, were relatively rare.

The purpose of this investigation is to marry the improved data assimilation technique with the I-T model (TIEGCM in this case) to better understand what physics drove the significant I-T responses observed locally by the three Fabry–Perot interferometers (FPIs) and Poker Flat Incoherent Scatter Radar (PFISR). Three FPIs located at Eagle (64.8°N, 141.2°W), Toolik (68.6°N, 149.6°W), and Kaktovik (70.1°N, 143.6°W), Alaska, all showed strong upward winds with maxima reaching an order of 50–100 m/s during the period of 08:30–09:30 Universal Time (UT) at ~250 km. Larsen and Meriwether (2012) reported that vertical winds with a magnitude of 10–20 m/s are common at high latitudes, while large vertical winds (up to 50 m/s) are often accompanied by substorm events at high latitudes or the generation of irregularities or sporadic layers at mid and low latitudes. Since the atmosphere is highly structured vertically, large vertical wind can cause significant displacement and mixing, thus plays an important role in the dynamics. The observations showing vertical winds larger than 50 m/s were relatively rare and deserve an investigation. In addition to the FPI measurements, the PFISR which is located at Poker Flat (65.1°N, 147.5°W), Alaska, had continuous measurements of electron densities (NE), line-of-sight ion drifts (VLOS) which can be used to derive electric fields, and ion and electron temperatures (TI and TE, respectively).

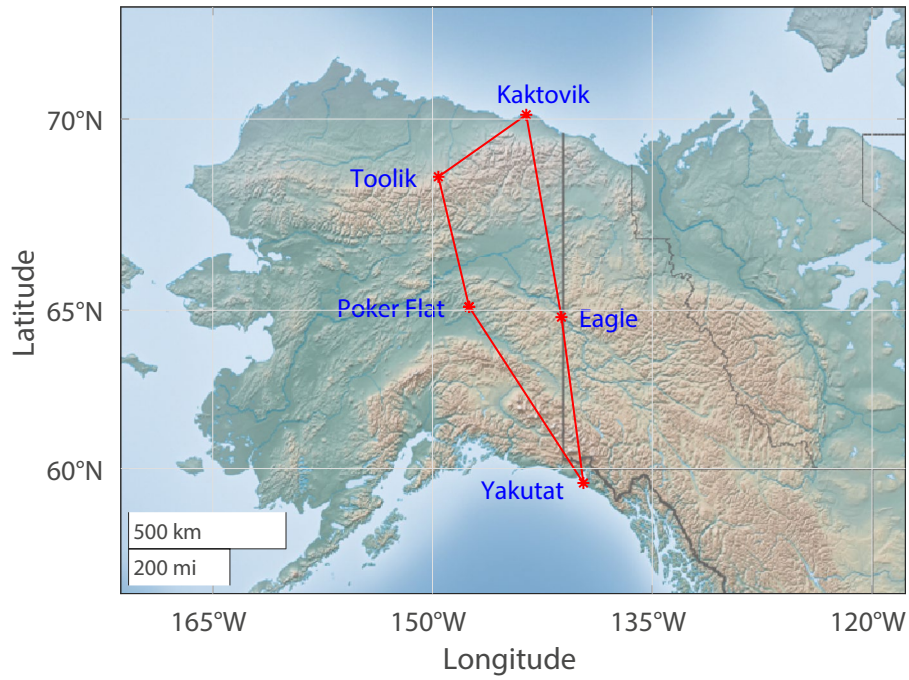

Figure 1. Geometry of the five observational stations in Alaska, including Poker Flat (65.1°N, 147.5°W), Eagle (64.8°N, 141.2°W), Toolik (68.6°N, 149.6°W), Kaktovik (70.1°N, 143.6°W), and Yakutat (59.5°N, 139.7°W).

The THEMIS/ASIs also had a decent coverage. The geometry of the above four stations along with an ASI site at Yakutat (59.5°N, 139.7°W), Alaska is shown in Figure 1. Such simultaneous observations of magnetospheric drivers (aurora and electric fields) and responses (neutral winds and ionospheric parameters) provide an excellent opportunity to constrain the I-T model at high latitudes, which can be further used to study the connections.

The paper is organized as follows. Data sources, assimilation method and different TIEGCM runs are introduced in Section 2. Model results along with the comparisons with data and key physical processes responsible for the strong upward winds and salient changes in the I-T system are discussed in Section 3. Discussion and conclusions are given in Section 4.

2. Ground-Based Observations, Data Assimilation, and TIEGCM Runs

2.1. St. Patrick's Day Storm and Ground-Based Observations

Figure 2 shows the geomagnetic indices on 17 and 18 March 2015. The geomagnetic storm starts at ~06:00 UT on March 17 as the interplanetary magnetic field (IMF) B_z turns south. The period of southward B_z lasts for almost a whole day before this parameter returns to zero at ~05:00 UT on 18 March, after which there are some minor fluctuations. IMF B_y turns to negative around 05:00 UT, 17 March, and lasts for 6 hr before becoming positive and lasting for another 12 hr. Solar wind velocities and densities show obvious enhancements during the southward B_z period (Figure 2b). Figure 2c shows auroral electrojet (AE) indices, which illustrate strong auroral activities after 06:00 UT and reach the first peak around 09:00 UT on 17 March. The symmetric horizontal component of geomagnetic field (SYM-H) index reaches a negative maximum (−230 nT) around midnight 17 March, and the storm remains in the recovery phase till midnight 18 March. Both IMF and AE indices show fast oscillations with periods of tens of minutes to an hour.

The simultaneous PFISR observations of ion drifts/electric fields at Poker Flat, Alaska, and neutral vertical wind measurements observed by the three FPIs are shown in Figure 3. During the period of 05:00–13:00 UT, PFISR was running at an experiment containing two long-pulse modes, which was suitable for the derivation of F-region parameters including NE, TI, TE, and VLOS. The F-region measurements use a long pulse with a 480 microsecond uncoded pulse and are gated to have a spacing of 36 km with a range resolution of 72 km, respectively. The E-region data presented are smeared due to ambiguity function associated with the long pulse, although

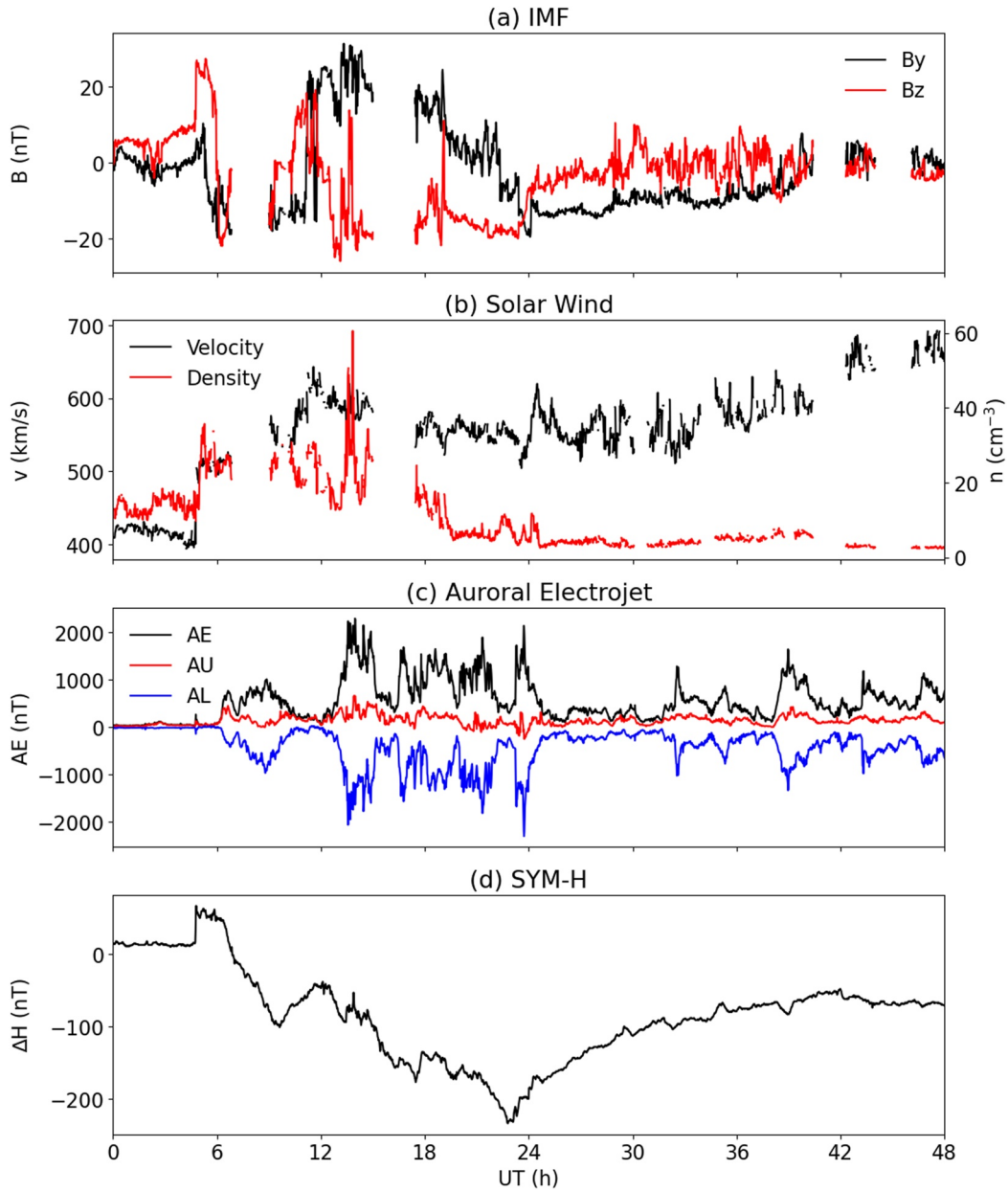

Figure 2. Geomagnetic indices on 17 and 18 March 2015: (a) interplanetary magnetic field B_y and B_z; (b) solar wind velocity and density; (c) auroral electrojet indices; and (d) SYM-H.

significant enhancements are captured. The methodology used to take the F-region VLOS observations and determine the plasma drifts is described in Heinselman and Nicolls (2008). Right after the storm onset, a strong westward ion drift with a magnitude of −1,800 m/s is detected around 06:30 UT corresponding to a northward E_y of ∼85 mV/m. After 08:00 UT, E_y switches to southward and maintains a significant magnitude of −50 mV/m which corresponds to an eastward ion drift of ∼1,000 m/s. Such southward E_y and eastward ion drift values last for nearly 2 hr until 10:00 UT. During this period (08:00–10:00 UT), the westward E_x increases to a magnitude of −30 mV/m (blue line in Figure 3b) along with strong southward ion drift (blue line in Figure 3a).

At the same time, the three FPIs all show sustained strong upward winds for a considerable period of time (from 08:30 to 10:00 UT). The peaks of the vertical winds (Wn) reach 50–100 m/s at Toolik and Kaktovik, and even exceed 100 m/s at Eagle. Around 06:00 UT, the FPIs observe strong downward neutral winds and reaches about −50 m/s. Even though the temporal evolutions of the three observations follow each other in general, the

10.1029/2022SW003308

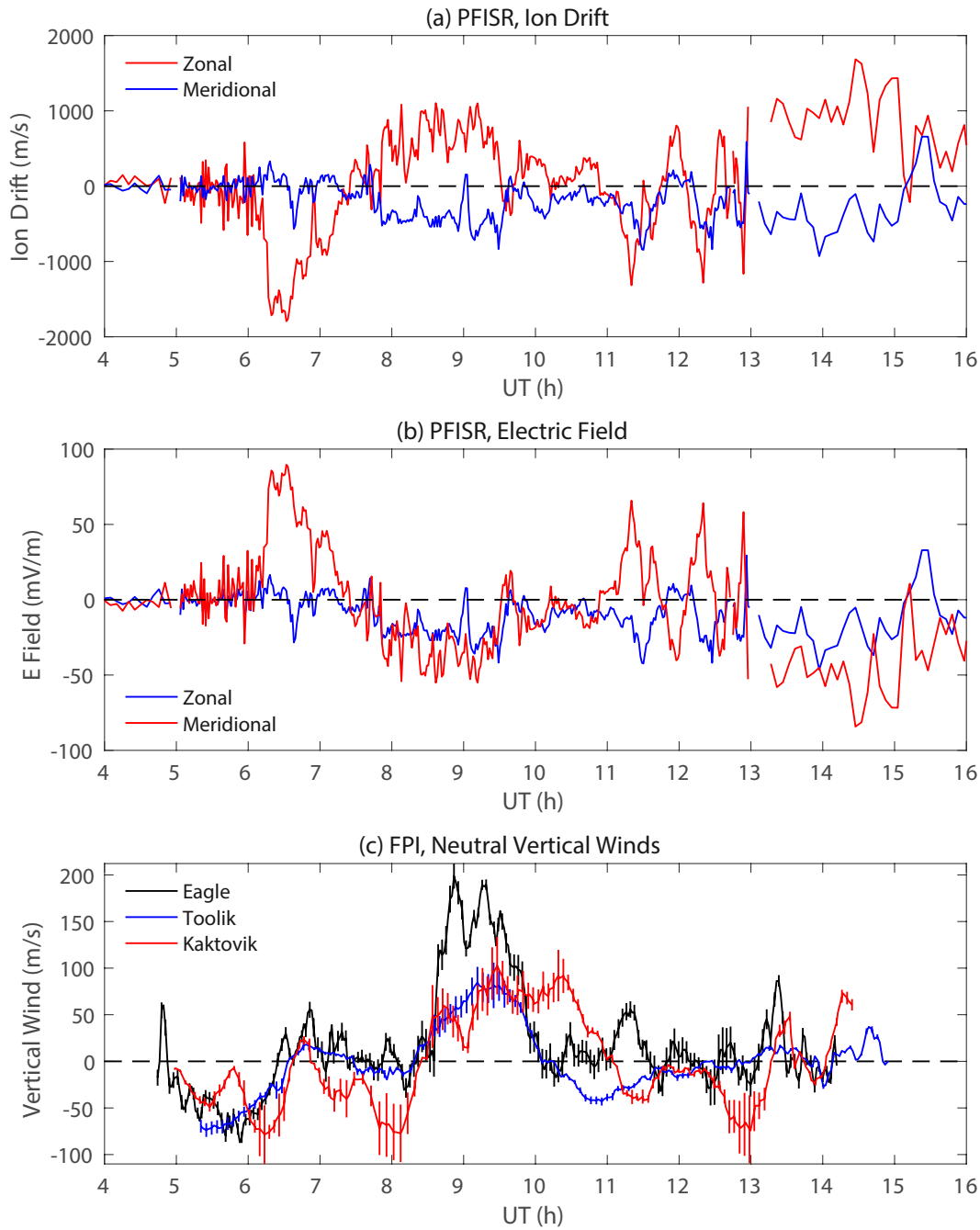

Figure 3. (a) Ion drifts, and (b) electric fields (zonal E_x, meridional E_y) observed by Poker Flat Incoherent Scatter Radar on 17 March 2015. (c) Neutral vertical winds measured by the Fabry–Perot interferometer at Eagle (black), Toolik (blue), and Kaktovik (red), Alaska, respectively. Vertical error bars denote for measurement uncertainties.

differences in wind magnitude and even direction at a particular time still exist. For instance, after 10:00 UT, the vertical wind keeps positive at Kaktovik, fluctuates around zero at Poker Flat, while turns into negative at Toolik, until 11:00 UT when they become both negative at Toolik and Kaktovik and turn back to positive at Poker Flat. Considering that the distances among these three stations are only about a few hundreds of kilometers (Figure 1), such local differences suggest that vertical winds are highly structured and characterized by mesoscale patterns.

In addition to electric fields and neutral vertical winds, discrete auroral activity is also intensified as captured by the THEMIS/ASIs (Mende et al., 2008). A substorm onset occurs at ~06:45 UT (a snapshot is shown in

10.1029/2022SW003308

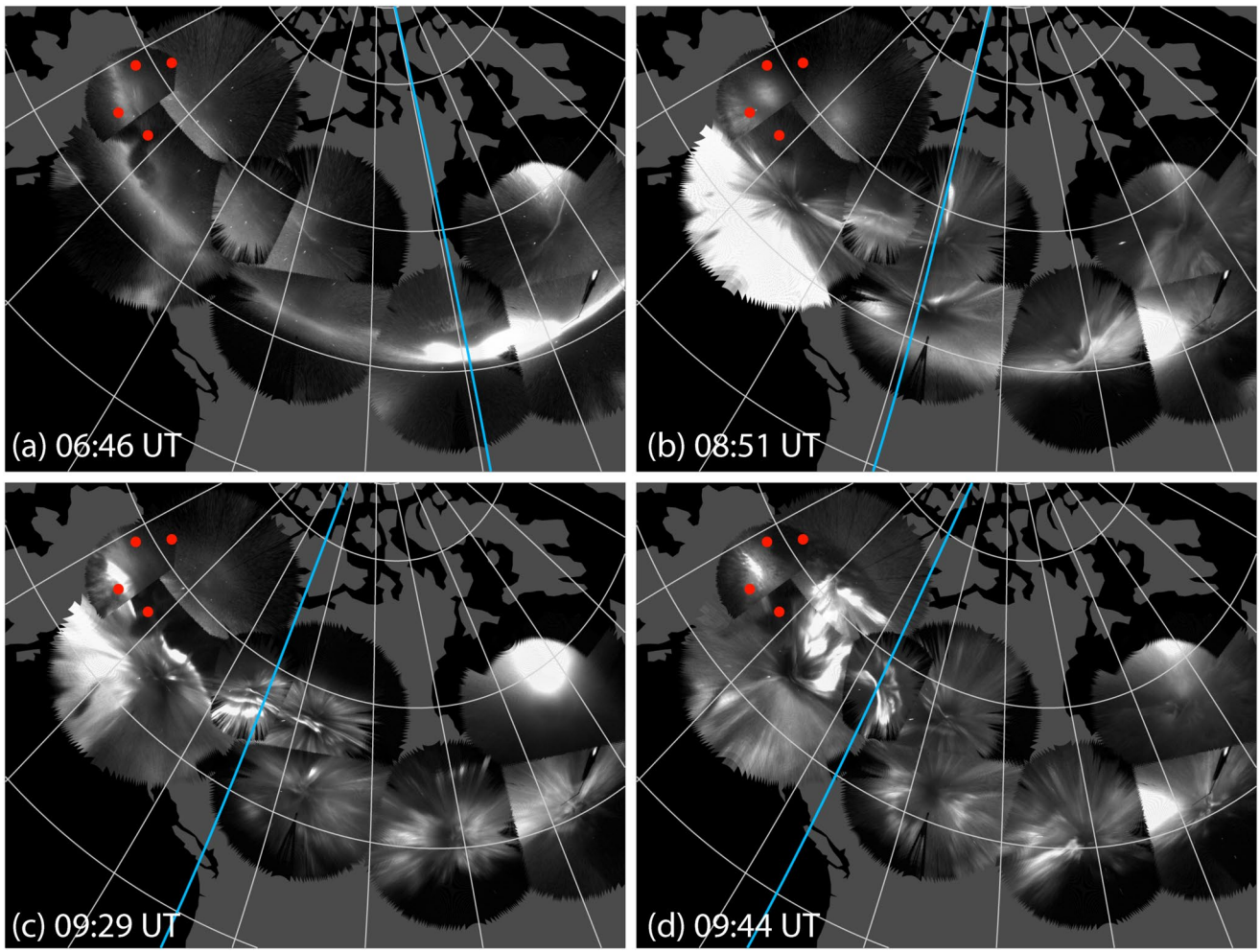

Figure 4. Evolution of aurora: white line emission (count/s) from Time History of Events and Macroscale Interactions during Substorms/all-sky imager observations. Four red spots denote for Poker Flat, Eagle, Toolik, and Kaktovik, Alaska.

Figure 4a), followed by a bulge expanding poleward and azimuthally toward the Alaska-Canada border. Another substorm onset occurs at ∼08:33 UT near Yakutat, Alaska with magnificent auroral emission and brightening lasting until ∼09:40 UT (Figures 4c and 4d), during which multiple intensifications of the bulge and auroral streamers appeared (Nishimura & Lyons, 2021) near Poker Flat and Eagle. Even though the sky was somewhat cloudy over Poker Flat which disabled the reliable derivation of energy flux and mean energy from the aurora emission, the raw images still show considerable aurora activity at Poker Flat during this substorm (Figures 4c and 4d), which lends confidence of padding aurora for Poker Flat in the data assimilation process (more details in Section 2.2). The precipitating energy flux and characteristic energy were obtained from the THEMIS ASI data (Nishimura & Lyons, 2021) and were incorporated into the data assimilation.

2.2. Data Assimilation for Aurora and Electric Fields

The Lattice Kriging modeling has been recently adopted for the data assimilation of aurora (Wu et al., 2022) and extended for the assimilation of electric fields (Wu & Lu, 2022). It has been shown to largely capture the temporal and spatial variability of real data. The field to be estimated is assumed to consist of a statistical mean, a variability term (spatially), and an error term. The empirical model can be used as the statistical mean with a scaling factor, for which we choose the Y. Zhang and Paxton (2008) model for aurora, which is built upon the historical Special Sensor Ultraviolet Spectrographic Imagers (SSUSI) observations and Kp driven, and the Weimer model (Weimer, 2005) for electric fields. The variability term is projected into the superposition of a series of radial basis functions (RBFs), which are more suitable to assimilate local features than the global spherical harmonic

fitting. The scaling factor and coefficients of RBFs are estimated from existing observations, which are then applied to reconstruct the field globally. The detailed mathematical formulation and principles can be found in Wu and Lu (2022) and Wu et al. (2022).

The SSUSI (Paxton & Meng, 1999; Paxton et al., 2002) onboard the DMSP and the THEMIS/ASI data are used for aurora assimilation. As shown in Figure 9 of Wu et al. (2022), the Lattice Kriging model can coherently combine the three data sets (empirical aurora model, SSUSI, and THEMIS/ASIs) with a smooth boundary transition and largely keep mesoscale features such as aurora arcs shown in the observations. The auroral image form Yakutat, Alaska (57°–61°N, 130°–140°W), is padded to a box of (65°–71°N, 140°–160°W) near Poker Flat, partially guided by the raw aurora images which illustrate that the temporal variations of aurora at these two locations are decently correlated (Figure 4). Such an implementation is proved to be reasonable by the comparison of TECs with Global Navigation Satellite System (GNSS) observations (Section 3.2). Without padding, the TECs at the northwest corner of Alaska including Poker Flat are too small compared with the GNSS observations, which implies that significant auroral activity is expected during the time of interest. Figure 5 shows the comparison of mean (characteristic) energy and number flux between the empirical model and data assimilation. The assimilated maps are more structured, and the magnitude of number flux calculated as energy flux divided by mean energy is significantly elevated due to the incorporation of the SSUSI and THEMIS/ASI observations which have much larger energy fluxes than the empirical model (Figures 5c and 5d). It is worth mentioning that the energy fluxes of THEMIS/ASIs need to be halved before feeding into the assimilation model in order to produce electron densities and TECs in the TIEGCM that match observations. The uncertainties of the measurements and of the ionization rate calculation in the model may cause this adjustment. Further work is needed to pinpoint the exact source.

The VLOS (converted to LOS electric fields) from the SuperDARN measurements and the PFISR observations of electric fields (Figure 3a) at Poker Flat (PFISR data are repeated in the ambient 4° × 4° region to ensure its weighting in the fitting) are used as data sources for the electric field assimilation. Wu and Lu (2022) have successfully extended the Lattice Kriging model to vector fields and they presented results from the same event. As shown in Figures 7 and 10 from Wu and Lu (2022), the assimilation results largely follow the PFISR observations locally and root-mean-square-errors (determined by the differences between assimilation and observations) decrease by more than half compared with the Weimer model. We show the comparison between the empirical and assimilated electric fields at 06:28 UT, when E_y reaches the maximum at Poker Flat, in Figure 6. The empirical model (Weimer, 2005) shows the large-scale patterns reasonably well while the assimilation results resolve much more finer structures. The empirical model shows positive E_y near Poker Flat with a much smaller magnitude versus the observation (Figure 6c vs. Figure 3b). After the data assimilation, the strong northward E_y is enforced near Poker Flat (Figure 6d), which helps to constrain the local electrodynamics. Since the SuperDARN data used for assimilation cover the high-latitude northern hemisphere reasonably well for this case (see Figure 4a in Wu and Lu (2022)), the assimilated results should in general impose more realistic electric fields than the empirical model, especially for the regions where the data are available. As shown in Figure 10 of Wu and Lu (2022), the short-term temporal variability (within an hour) of electric fields from the PFISR observations is also captured in the data assimilation.

2.3. Four TIEGCM Runs

TIEGCM is a global 3D numerical model that simulates the coupled thermosphere/ionosphere system from ~97 to ~600 km altitude. It self-consistently solves the fully coupled nonlinear, hydrodynamic, thermodynamic, and continuity equations of the neutral gas, the ion and electron energy equations, the O^+ continuity equation and ion chemistry, and the neutral wind dynamo (Qian et al., 2014; Richmond et al., 1992). In this study, the resolution of TIEGCM is 1.25° × 1.25° × 1/8 scale height in latitude × longitude × altitude (Dang et al., 2018, 2021). Realistic F10.7 are used in all simulations. Realistic IMF conditions are used to drive the Weimer model for the empirical high-latitude electric field run. The time step of the TIEGCM simulation is 10 s. The output frequency of the diagnostic terms is 1 min.

In the current study, both aurora and electric field have two types of maps, one from the empirical model and the other one from the data assimilation, which gives rise to a combination of four options for high-latitude drivers. These four options are used to drive the TIEGCM. We list the names (R1–R4: $R_{a\_emp\_e\_emp}$, $R_{a\_assi\_e\_emp}$, $R_{a\_emp\_e\_assi}$, and $R_{a\_assi\_e\_assi}$) and the corresponding setups for the auroral and electric field drivers of these four runs in Table 1.

10.1029/2022SW003308

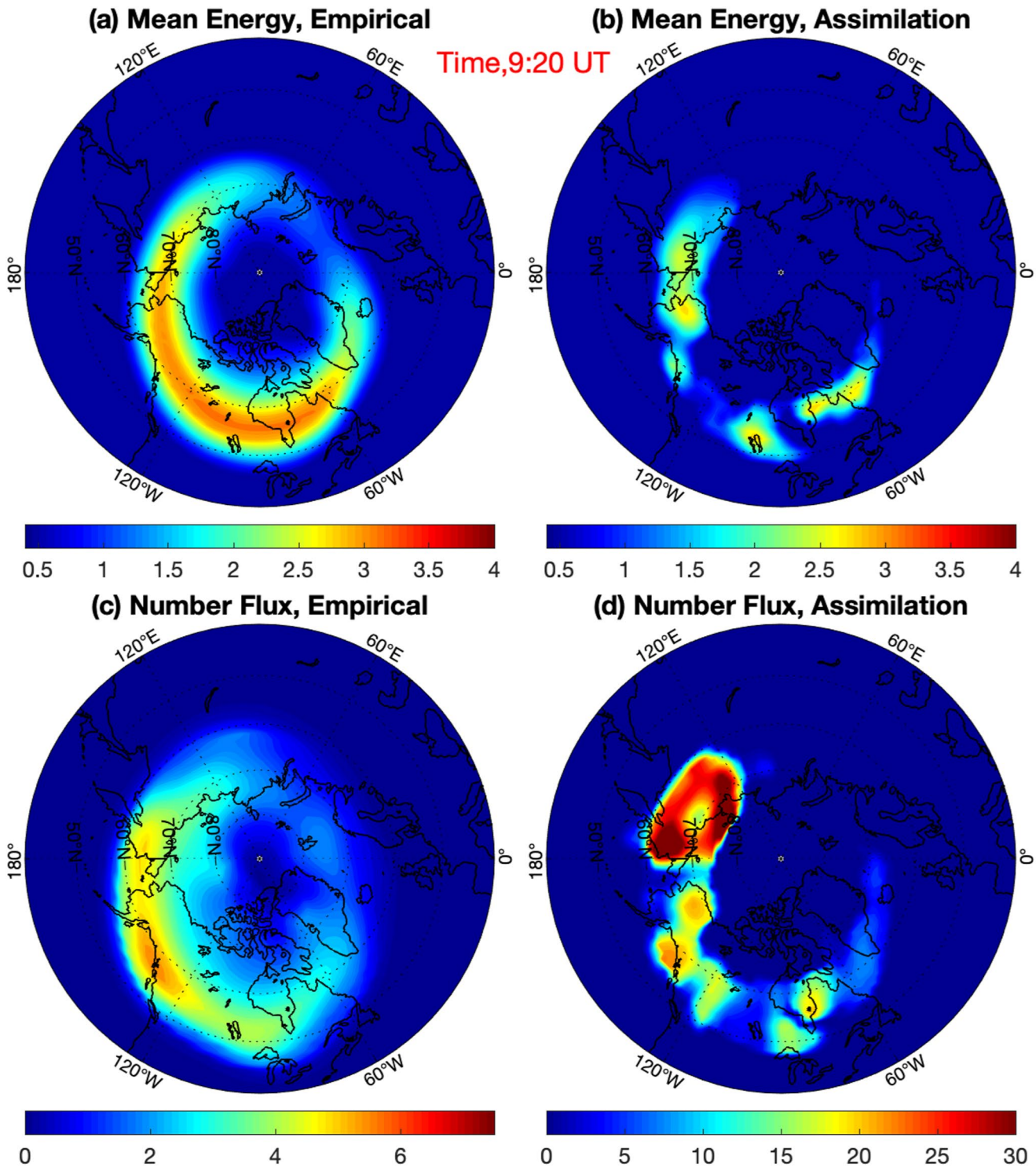

Figure 5. (a, b) Aurora mean energy (keV) maps at 09:20 Universal Time from the empirical model (Y. Zhang & Paxton, 2008) and assimilation, respectively. (c, b) Are the same except for the number fluxes (10^8/cm^2/s). Note the colorbars of panels (c and d) are different. All these maps are the ones used to drive different Thermosphere Ionosphere Electrodynamics General Circulation Model runs.

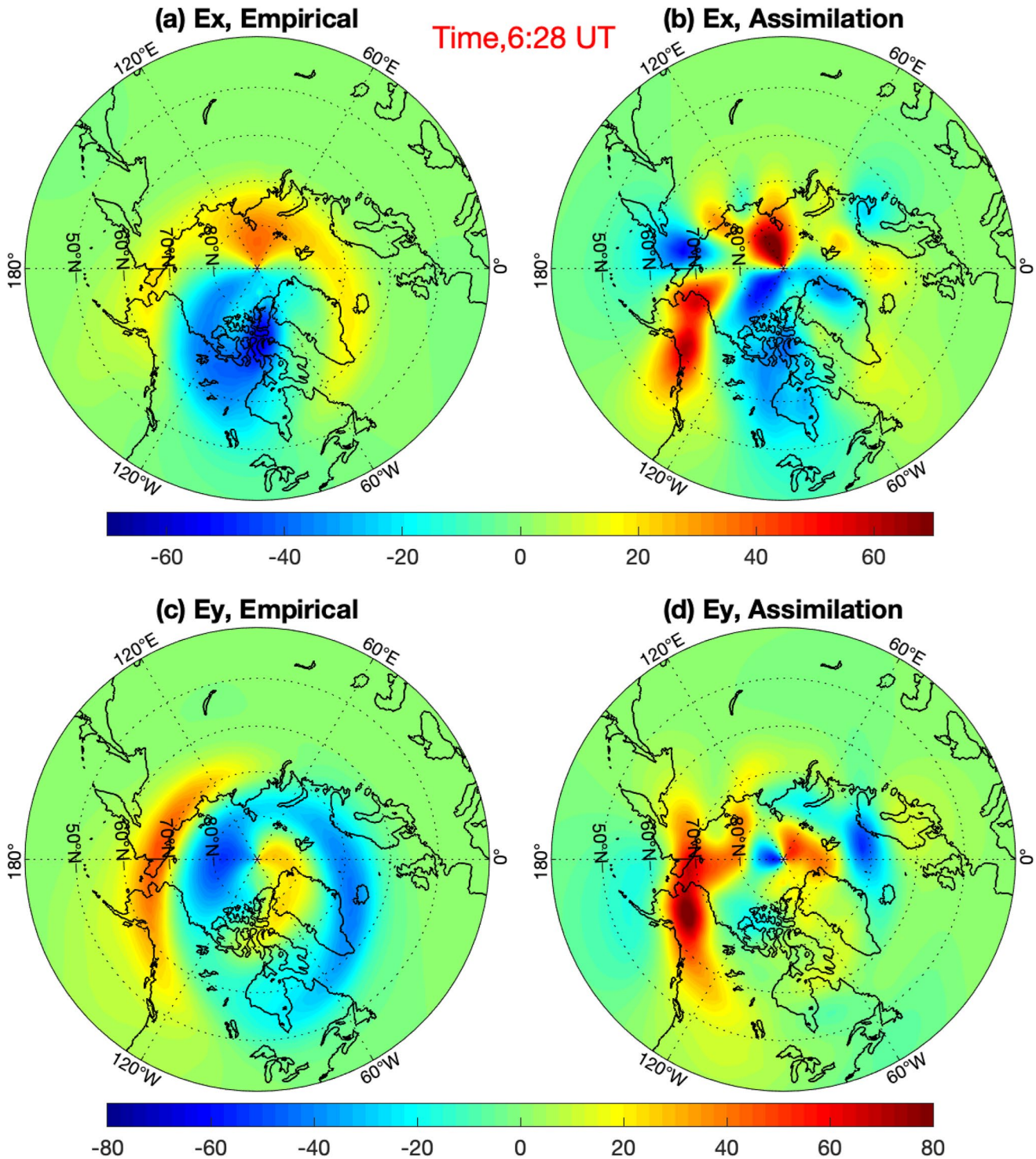

Figure 6. (a, b) E_x and (c, d) E_y at 06:28 Universal Time, respectively. (a, c) Are from the empirical Weimer model, while (b, d) are from the data assimilation. The unit is mV/m.

3. Model Results, Model-Data Comparisons, and Mechanism Studies

3.1. Local Neutral and Ionospheric Responses

Before we compare the modeled neutral and ionospheric responses among the four different TIEGCM runs, we show the PFISR measurements of electron density (NE), electron temperature (TE), and ion temperature

Table 1
Names and Setups for the Auroral and Electric Field Drivers for the Four Different Thermosphere Ionosphere Electrodynamics General Circulation Model Runs. "a" and "e" Are the Short Names for "Aurora" and "Electric Field", Respectively; "Emp" and "Assi" Are the Short Names for "Empirical Model" and "Assimilated Results," Respectively

	R1: $R_{a\_emp\_e\_emp}$	R2: $R_{a\_assi\_e\_emp}$	R3: $R_{a\_emp\_e\_assi}$	R4: $R_{a\_assi\_e\_assi}$
Aurora	Empirical	Assimilated	Empirical	Assimilated
Electric fields	Empirical	Empirical	Assimilated	Assimilated

(TI) to provide an observational baseline (Figure 7). The most prominent feature in NE compared with the quiet-time (not shown here) is the secondary peak formation (around 150–200 km) during the period of 09:00–10:30 UT (black rectangular in Figure 7a), most likely produced by auroral particle precipitation. The timing is consistent with the THEMIS/ASI observations of aurora surge and brightening (Figure 4, Section 2.1). Ion temperatures show significant elevation and reach ~3500 K around 06:30 UT (Figure 7c), concurrent with the occurrence of strong E_y (Figure 3b) and indicative of a strong frictional heating. It is intriguing that the strongest enhancement of TI occurs in the altitude range below 250 km. Electron temperatures also increase compared to the quiet-time and two most significant heating periods occur around 06:30 and 09:00 UT, when either electric field or aurora is intensified. Different from the enhancement of ion temperatures which maximizes around 150–200 km near 06:30 UT, the enhancement of electron temperatures generally increases with altitude. Around 08:00, 08:30, 09:00, 09:45, 11:30, 12:20, and 12:40 UT, both ion and electron temperatures show significant increases especially above 250 km. All the three quantities (Ne, TE, and TI) show oscillations with periods of tens of minutes to an hour, which are in compliance with the periodicity of the magnetospheric forcing (Figures 2 and 3).

We illustrate TI, TE, and NE from the four different TIEGCM runs at Poker Flat in Figures 8–10, respectively. Figures 8a, 9a, and 10a, show the results from the default TIEGCM run (R1) driven by empirical aurora and empirical electric fields. The R1 simulation fails to reproduce the observed features for all the three quantities: TI and TE do not show significant increases and NE does not capture the secondary peak compared to the PFISR observations. From Figure 8, the differences between R1 and R2, and R3 and R4, are trivial, which suggests that electric fields are the most important factor for enhanced ion temperature during the storm-time. This is sensible since ion frictional heating which dictates the ion temperature, is proportional to the square of the electric field magnitude. Both auroral particle precipitation and the electric field affect TE (Figure 9). Even though aurora assimilation enhances TE during the period of 08:30–11:00 UT around 250 km (Figure 9b), the most significant heating effect originates from the assimilation of the electric field, by comparing Figures 9a, 9c, and 9d.

NE can be affected by both aurora and electric field (Figure 10), even though aurora seems to be the key for the formation of the secondary peak in the upper E and lower F regions (Figures 10b and 10d). The aurora assimilation leads to a stronger particle precipitation locally, which increases ionization rate and thus causes the enhancement in electron densities. By comparing Figure 10a with Figures 10c and Figure 10b with Figure 10d, which differ solely by electric fields, the empirical electric field model (Weimer in this case) tends to overestimate NE. There are two processes potentially affecting local electron densities at Poker Flat:1) electric fields lead to Joule heating causing an upwelling in the thermosphere changing composition with a depleted O/N_2; and (b) electric fields can transport the plasma in/out of the region to introduce temporal variations and therefore change local electron densities.

We compare the neutral vertical winds in Figure 11. We first compare the simulations at Poker Flat from the four different runs (Figure 11a1–11a4). From the runs driven by the empirical electric fields (R1 and R2), vertical winds are rather small below 300 km. The assimilation of electric fields introduces stronger vertical winds and more temporal variability (Figures 11a3 and 11a4). R4 assimilates both aurora and electric field and generates the strongest vertical winds below 300 km. In particular, the enhancement of vertical winds of the order of 40 m/s during the period of 08:30–09:30 UT below 300 km is only captured by R4, implying that both aurora and electric field are responsible for the strong upward vertical winds.

We compare the neutral vertical winds from R1 and R4 for the three FPI stations (Eagle, Toolik, and Kaktovik) in Figures 11b1, 11b2, 11c1, 11c2, 11d1, and 11d2, respectively. Similar to Poker Flat, the vertical winds are significantly strengthened and show temporal variabilities. During the period of 8:30–10:00 UT, strong upwelling winds are found especially for Toolik, which reaches ~60 m/s and are quite comparable with observations (Figure 3c). Note that the local measurements of aurora and electric fields were not available for the assimilation for the FPI locations and considering the fact that magnetospheric energy input can be structured, the exact matching with the FPI observations is not required in this study. The overall improvement of the magnitude and variability in neutral vertical winds is clearly achieved.

According to Figure 5 in Wu et al. (2020), the strong Joule heating in the 100–150 km region causes a significant increase in the neutral temperature above this altitude range. This thermal enhancement is responsible for the

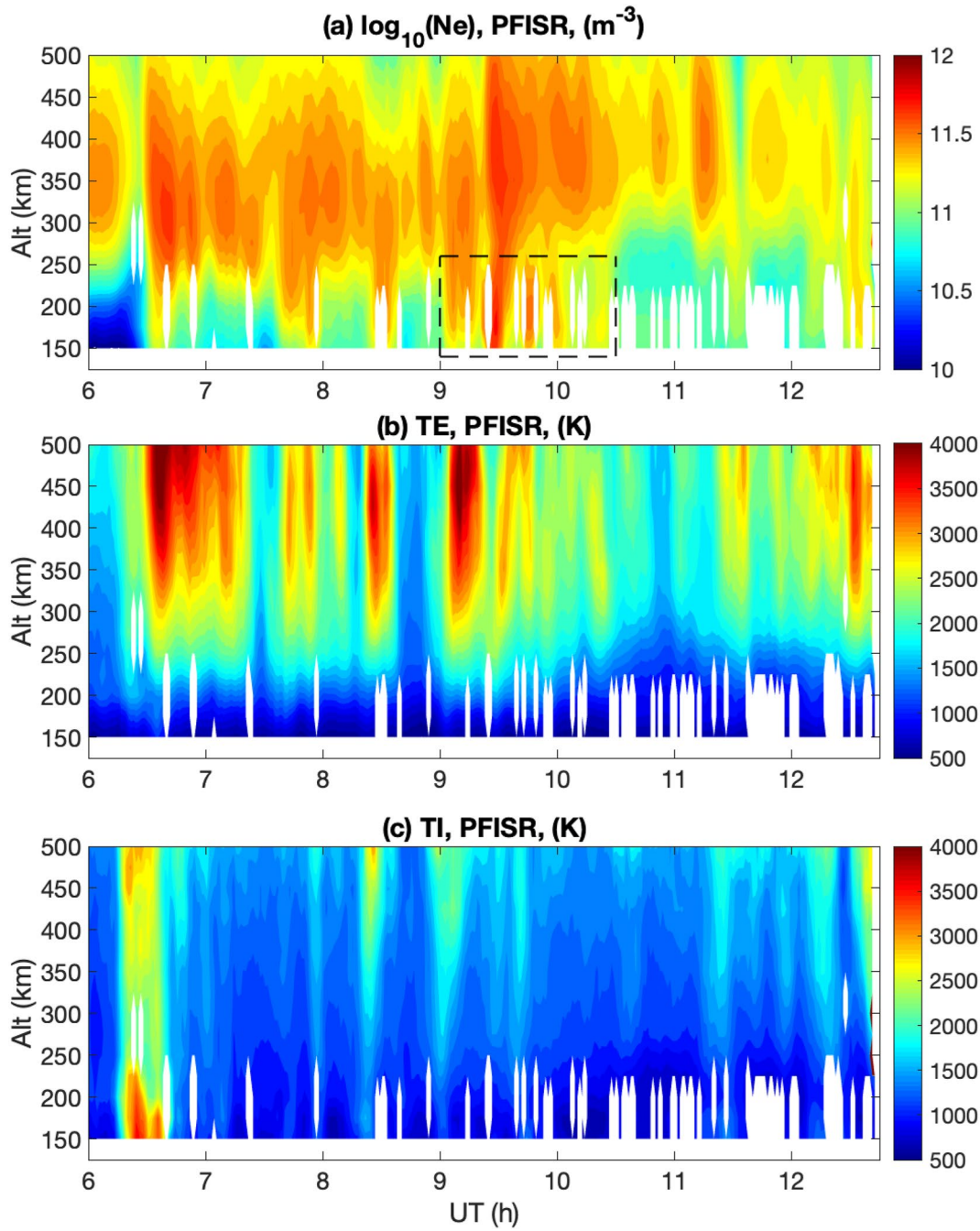

Figure 7. (a) Electron density (NE), (b) electron temperature, and (c) ion temperature observed by Poker Flat Incoherent Scatter Radar on 17 March 2015. The dashed black rectangular in panel (a) highlights the occurrence of the secondary peak in NE.

TTEIL, and the generation of strong vertical winds (~100 m/s) above. To simulate the TTEIL and produce better agreement with the lidar observations, the authors had to incorporate the realistic SSUSI aurora precipitation and sub-grid electric field variability in order to gain the necessary magnitude of Joule heating. In the current study, we implement the data assimilation of aurora and electric fields for the same purpose, that is, to reproduce more realistic Joule heating locally and the resulting effects on neutral temperatures and winds.

Figure 12 shows the comparisons of Joule heating rate per unit mass (W/kg) at Poker Flat from the four runs and for the three FPI stations from R1 and R4. The differences are introduced mainly by electric fields. The Joule heat-

10.1029/2022SW003308

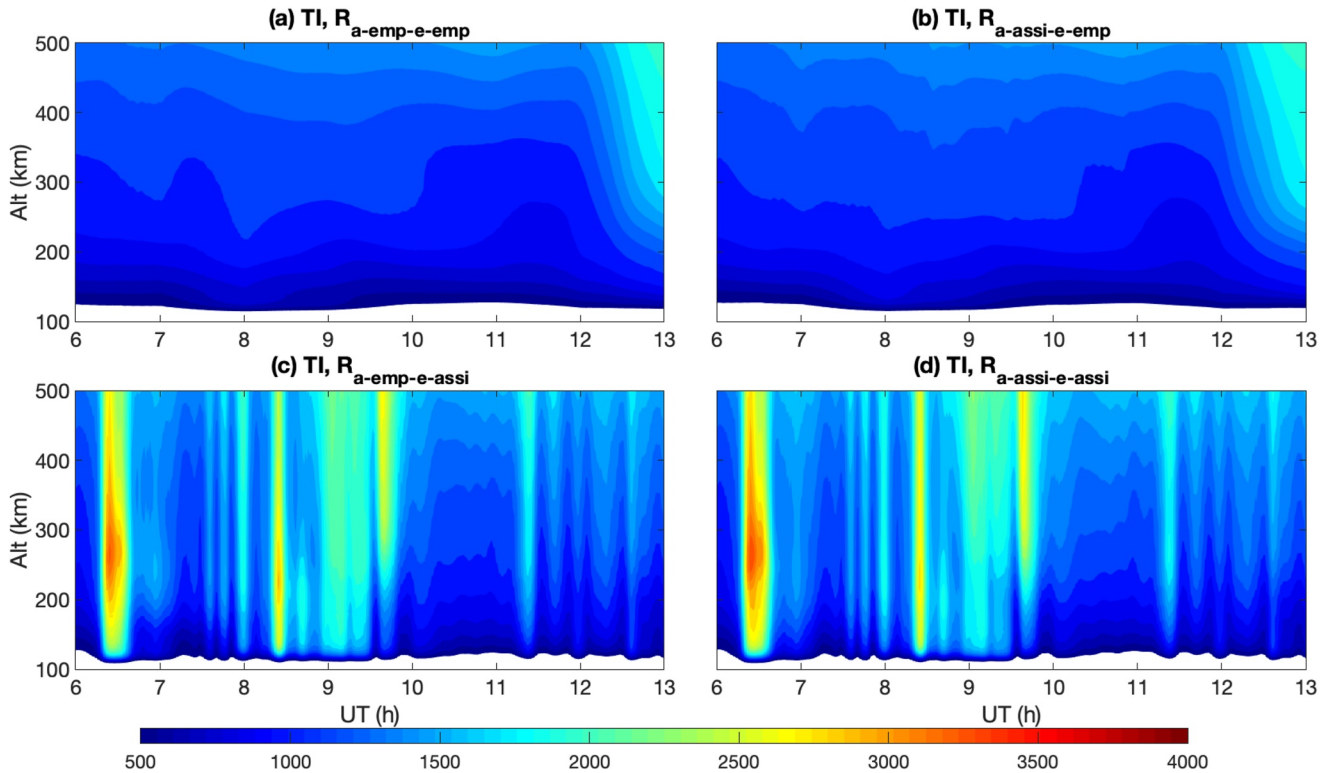

Figure 8. Thermosphere Ionosphere Electrodynamics General Circulation Model simulations of ion temperatures at Poker Flat from the four different runs. Unit is K.

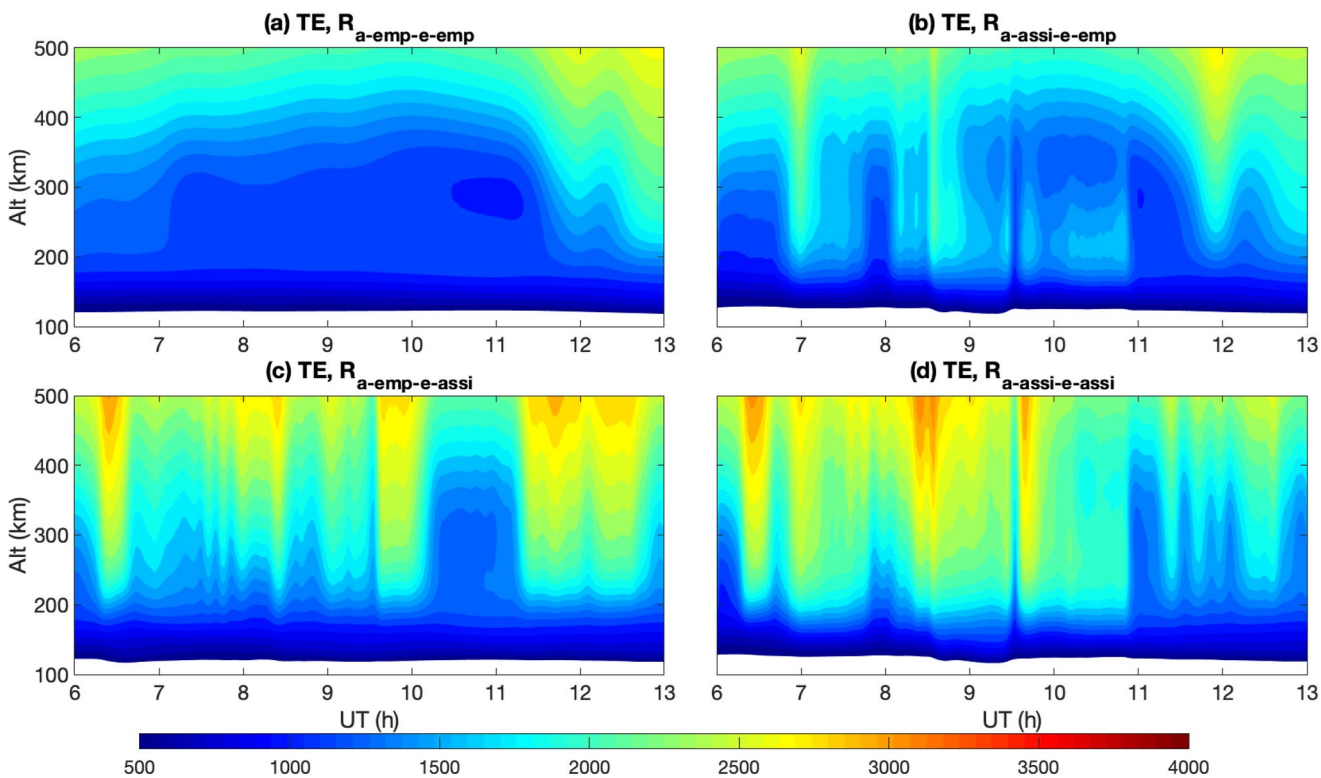

Figure 9. Similar to Figure 8 except for electron temperatures (K).

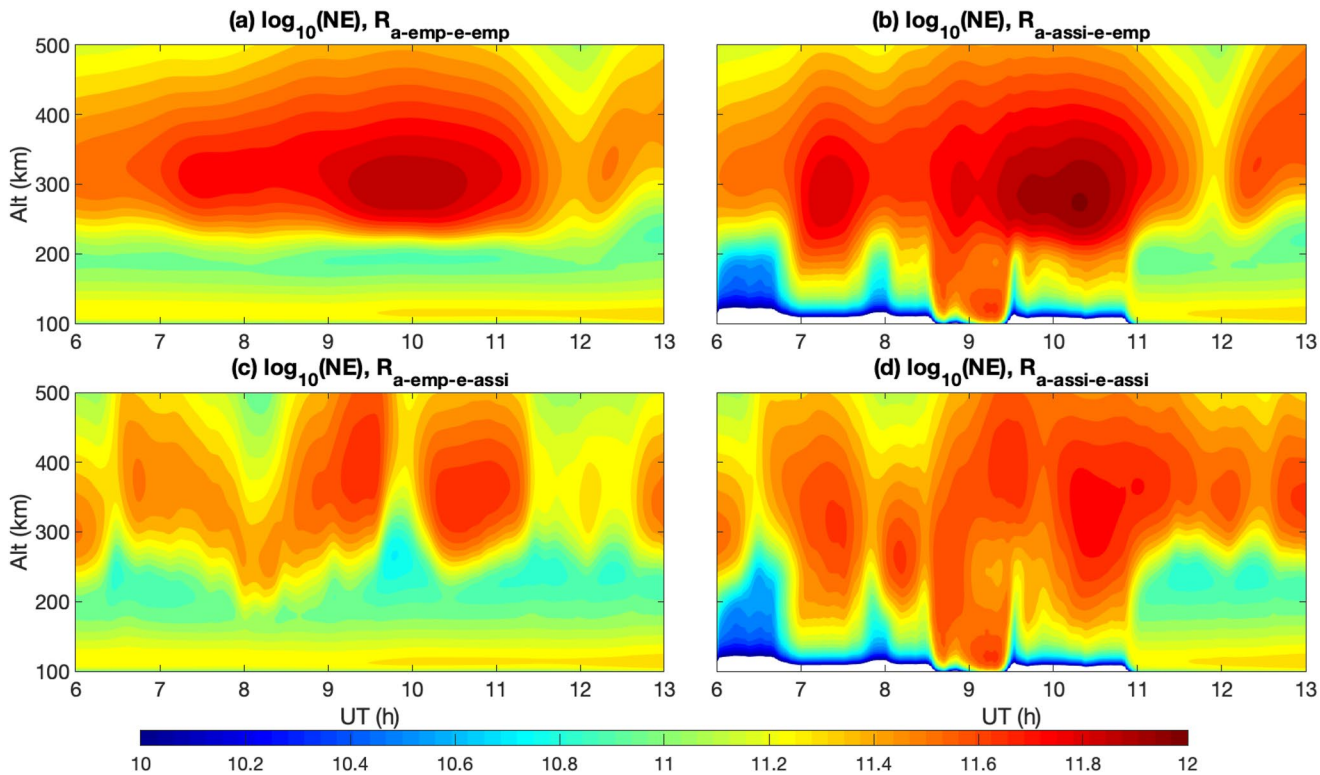

Figure 10. Similar to Figure 8 except for electron densities (1/m^3).

ing rate also shows short-term temporal variations (order of minutes). Significant Joule heating around 06:30 UT (Figures 12a3 and 12a4) associated with the strong E_y (red line in Figure 3b) explains the sharp increases of TI at the same time observed by PFISR (Figure 7c) and simulated by the run with assimilation (R4, Figure 8d). Compared with the Joule heating around 06:30 UT which mainly concentrates in the F region, the strong aurora activity around 09:00 UT leads to the relatively strong Joule heating in the lower E-region (red rectangles in Figure 12), which corresponds reasonably well with the strong upwelling above (black rectangle in Figure 11). By cross-comparing Figures 12a1–12a4, both aurora and electric field which become strong around 09:00 UT are responsible for the increase of the magnetospheric energy deposition, inducing the strong upward vertical wind. Such a heating process is regional and at least partially responsible for the strong upward winds in the other three stations.

We compare the height-integrated Joule heating rate at Poker Flat and the maximum integrated Joule heating rate at high northern latitudes (>50°N) in Figure 13. The significant local enhancement associated with the data assimilation at Poker Flat is salient, which indicates that the default model run driven by empirical magnetospheric drivers misses the characterization of localized energy deposition. The magnitudes of the maximum height-integrated Joule heating rate over the globe (>50°N), however, are more comparable among the four different runs, except that the assimilation runs show stronger peaks and more temporal variability driven by observational data. Such comparisons suggest that the data assimilation has guided the spatial distribution of energy deposition and led to different locations that peak in Joule heating. The large Poynting flux exceeding 100 mW/m^2 has been observed by the DMSP F13 during a strong magnetic storm (C. Y. Huang & Burke, 2004). D. Knipp et al. (2011) has also reported a day-side Poynting flux as large as 170 mW/m^2 occurring during the period of high-speed solar winds. It is noted that the majority of Poynting flux is transferred to Joule heating in the upper atmosphere (G. Lu et al., 1995; Thayer & Semeter, 2004). Thus the magnitude of the integrated Joule heating rate simulated in this study is within a reasonable scope.

In order to further quantify the improvements introduced by the assimilated drivers compared to the empirical ones, we provide two metrics, maximum values and root-mean-square (rms) errors, for Ne, Te, Ti, and Wn (Table 2). For Ne, Te, and Ti, the rms errors are calculated from the differences between each model run and PFISR observation. All the time-altitude points with valid observations are considered. For the rms error of Wn, the model data at ~250 km is extracted first and the difference from FPI measurements is used for calculation. We use Toolik as an example in

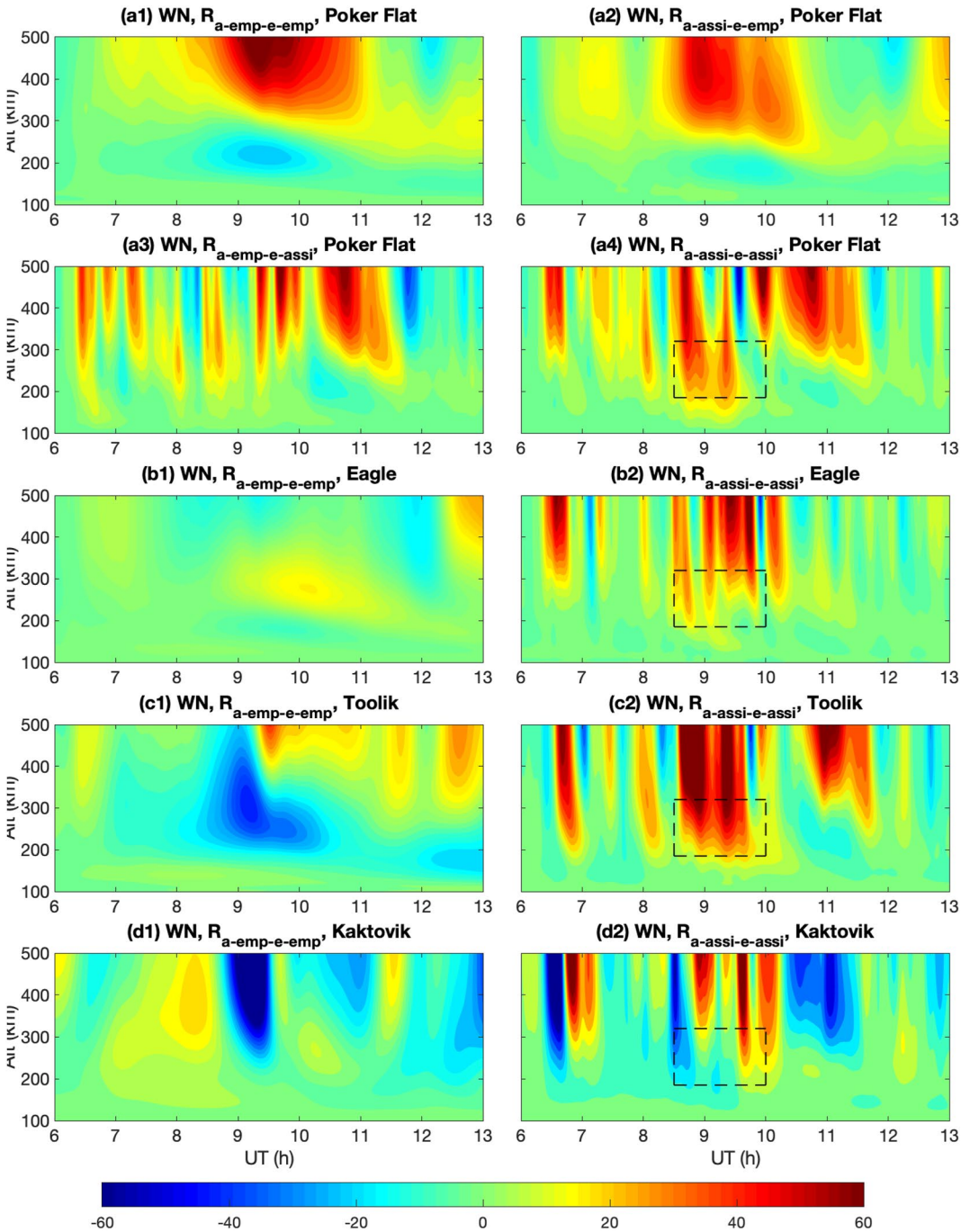

Figure 11. Similar to Figure 8 except for vertical winds (m/s). The black dashed rectangle highlights the period with enhanced vertical winds around 250 km.

Table 2. There is a clear trend that maximum values increase and become the closest to the observations as both aurora and electric fields are assimilated. At the same time, rms errors decrease by 30%–50% depending on physical quantity, indicating that model results better match observations, especially as the electric field assimilation is implemented.

3.2. Regional to Global Neutral and Ionospheric Responses

Since the data assimilation considers SSUSI and THEMIS for aurora, and SuperDARN for electric fields, which have a substantial spatial coverage, it should lead to an overall improvement of regional or even global simulations. Figure 14 shows the TEC distributions from the four runs compared with the GNSS observations. With the

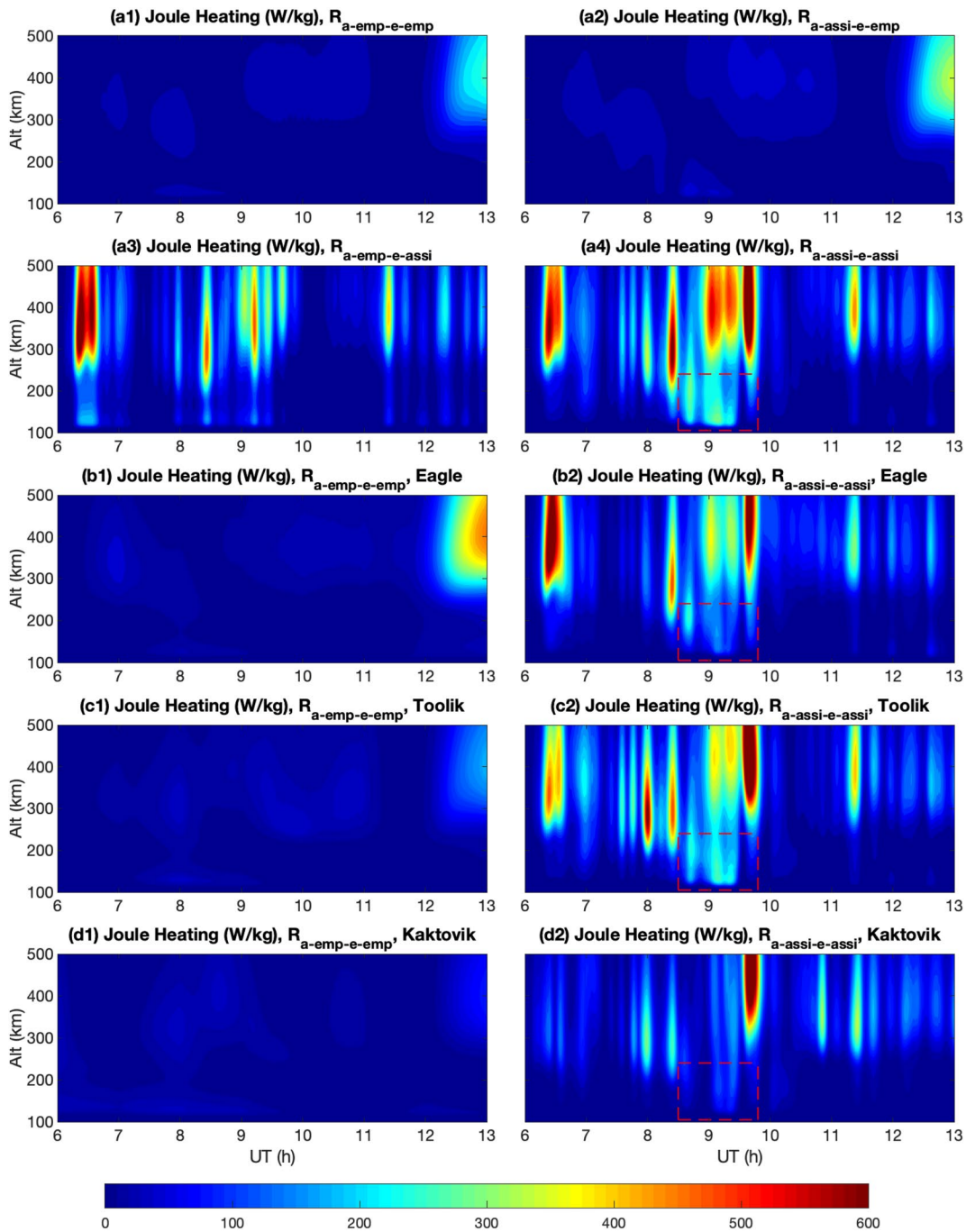

Figure 12. Same as Figure 11 except for altitude-resolved Joule heating. The red dashed rectangle highlights the period with the significant Joule heating to the E-region.

realistic aurora (R2 and R4), the TECs from Alaska circling to the Great Lake regions are elevated, which follow the enhancement of aurora energy flux shown in Figure 4. R2 tends to overestimate the TEC in Alaska while R4 matches the GNSS observations the best especially in the magnitude, consistent with the local simulation of TEC that empirical electric field run leads to a larger NE (Figure 10). A movie showing the TEC comparison with time is provided in Supporting Information S1, which illustrates that R4 mostly captures the temporal evolution of TECs as observations, and such improvement lasts for the whole period of the storm.

A better representation of the time, location and strength of energy deposition with data assimilation leads to the differences in the simulated neutral dynamics and winds from different runs. To explore this, we examine the

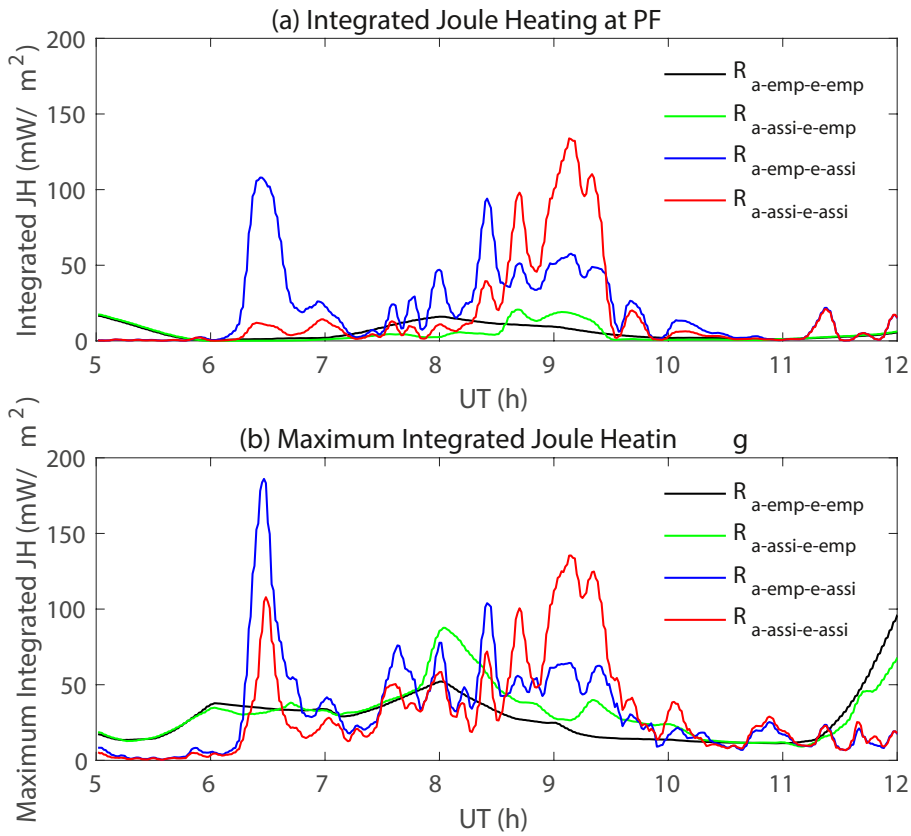

Figure 13. (a) Comparison of height-integrated Joule heating (mW/m^2) at Poker Flat from the four Thermosphere Ionosphere Electrodynamics General Circulation Model runs. (b) Same as (a) except for the maximum height-integrated Joule heating at high latitudes (>50°N) of the northern hemisphere.

signal of traveling atmospheric disturbances (TADs) from neutral vertical winds. According to the dispersion relation of gravity waves, vertical wind can better manifest higher-frequency and smaller-horizontal scale waves than horizontal winds and temperature (X. Lu et al., 2015, 2017; Vadas, 2013). Figure 15 shows the vertical winds from R1 and R4 at ~250 and ~550 km altitudes at 09:45 UT and the movie (included in Supporting Information S1) shows their temporal evolutions. The TADs are always stronger and can reach lower latitudes in R4 than in R1, especially at ~550 km. This means that the wave source for TADs is stronger, and neutral responses to the storm are more dynamic in R4, characterized by richer scales and broader extension, than those captured by the default model run. In order to quantify such effects, we compute the longitudinal variability (calculated as the standard deviation along longitude) of vertical winds as a function of latitude and UT, and temporal variability as a

Table 2
Improvement Metrics of Assimilation Runs Compared to the Empirical Runs

		Run 1	Run 2	Run 3	Run 4	Observation
Ne (1/m^3)	Max (<200 km)	2.1×10^{11}	4.7×10^{11}	2.0×10^{11}	4.7×10^{11}	5.2×10^{11}
	RMS error	2.0×10^{11}	2.5×10^{11}	1.0×10^{11}	1.5×10^{11}	
Te (K)	Max	2760	2710	3080	3260	4440
	RMS error	763	681	486	505	
Ti (K)	Max	1980	2010	3350	3400	3310
	RMS error	458	445	342	330	
Wn (m/s)	Max	3.6	10.0	48.5	58.8	84.5
	RMS error	47.7	38.4	30.0	23.3	

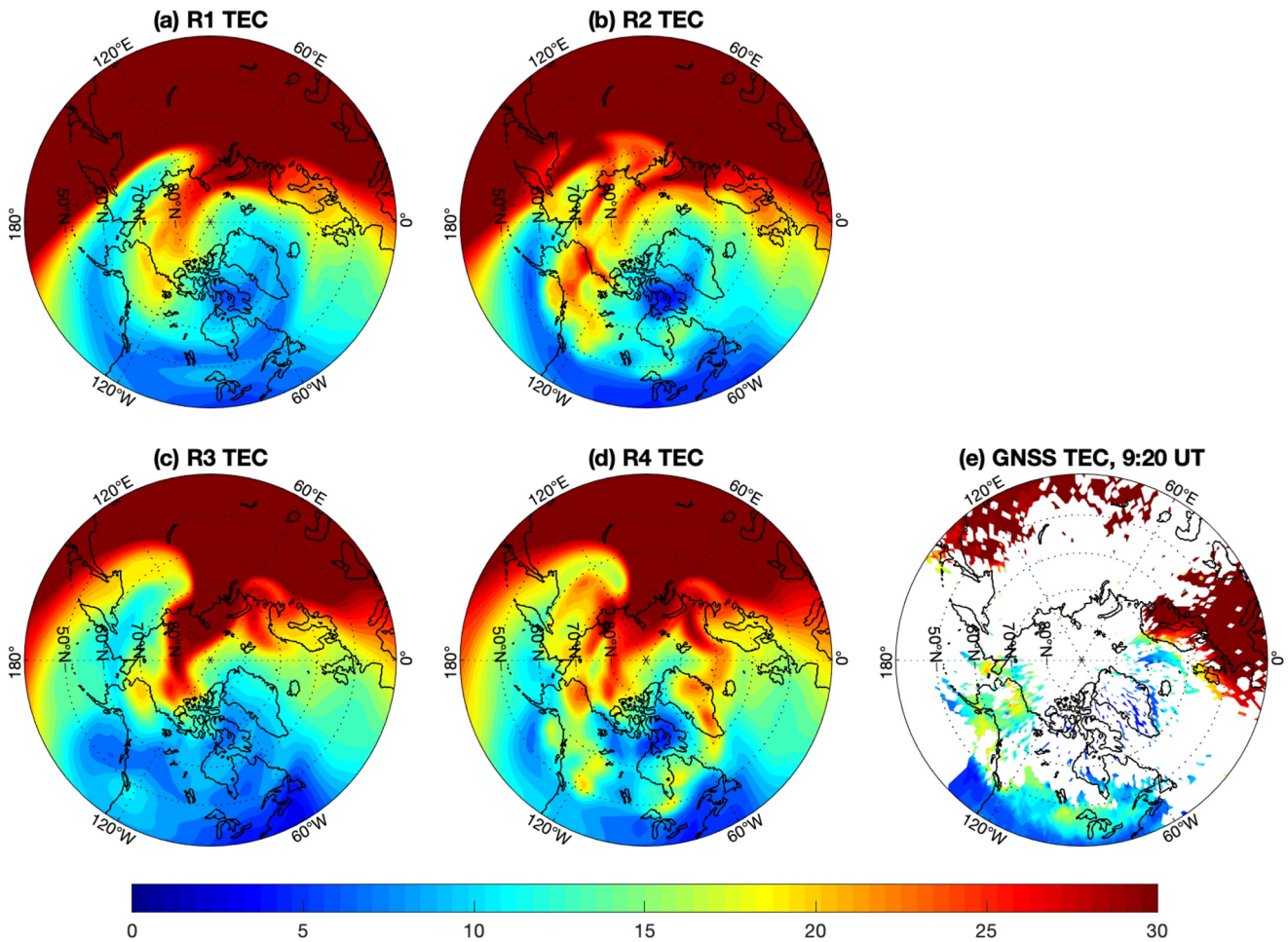

Figure 14. Model simulations of Total Electron Content (TEC) (unit: TECu) compared with Global Navigation Satellite System (GNSS) TEC observations at 09:20 Universal Time (UT). (a–d) TEC simulation from R1 ($R_{a\_emp\_e\_emp}$), R2 ($R_{a\_assi\_e\_emp}$), R3 ($R_{a\_emp\_e\_assi}$), and R4 ($R_{a\_assi\_e\_assi}$), respectively. (e) GNSS TEC observations at 09:20 UT. The movie about this comparison is provided in Supporting Information S1.

function of latitude and longitude. Figure 16a1–16d1 show longitudinal variabilities for the four runs. Figure 16e1 shows the time-averaged means of the longitudinal variabilities from the four runs. Figure 16a2–16d2 show temporal variabilities of vertical winds, and Figure 16e2 shows their zonal means. In general, the assimilated electric fields are more important than aurora to increase the spatial and temporal variabilities. For the time-averaged spatial variability (Figure 16e1), R4 shows a larger magnitude by a factor of 1.5–3 compared to R1 (default run), depending on latitude. And for the zonal-mean temporal variability (Figure 16e2), R4 is also larger than R1 by a factor of 1.5–3. Such ratios suggest that the wave activities (TADs) are stronger, embrace more short-term temporal and small-scale spatial scales, in the data-assimilation run than in the default one.

4. Discussion and Conclusions

We apply the newly implemented Lattice Kriging model to assimilate both aurora and electric fields for the 2015 St. Patrick's Day storm, use them to drive the TIEGCM, and produce more realistic I-T system responses than the default run that is driven with empirical high-latitude inputs. The improvement of model simulation enabled by data assimilation includes: (a) higher TI and TE (up to ~3000 K) due to the enhancement of local heating; (b) larger NE below 200 km and the emergence of the secondary peak in the upper E and lower F region around 09:00 UT when aurora surges occur; (c) stronger neutral vertical winds around 250 km due to large Joule heating below that caused by both the intensified aurora and enhanced electric fields; (d) enhanced TECs around auroral oval because of the auroral particle precipitation; and (e) a larger amplitude of TADs and further extension

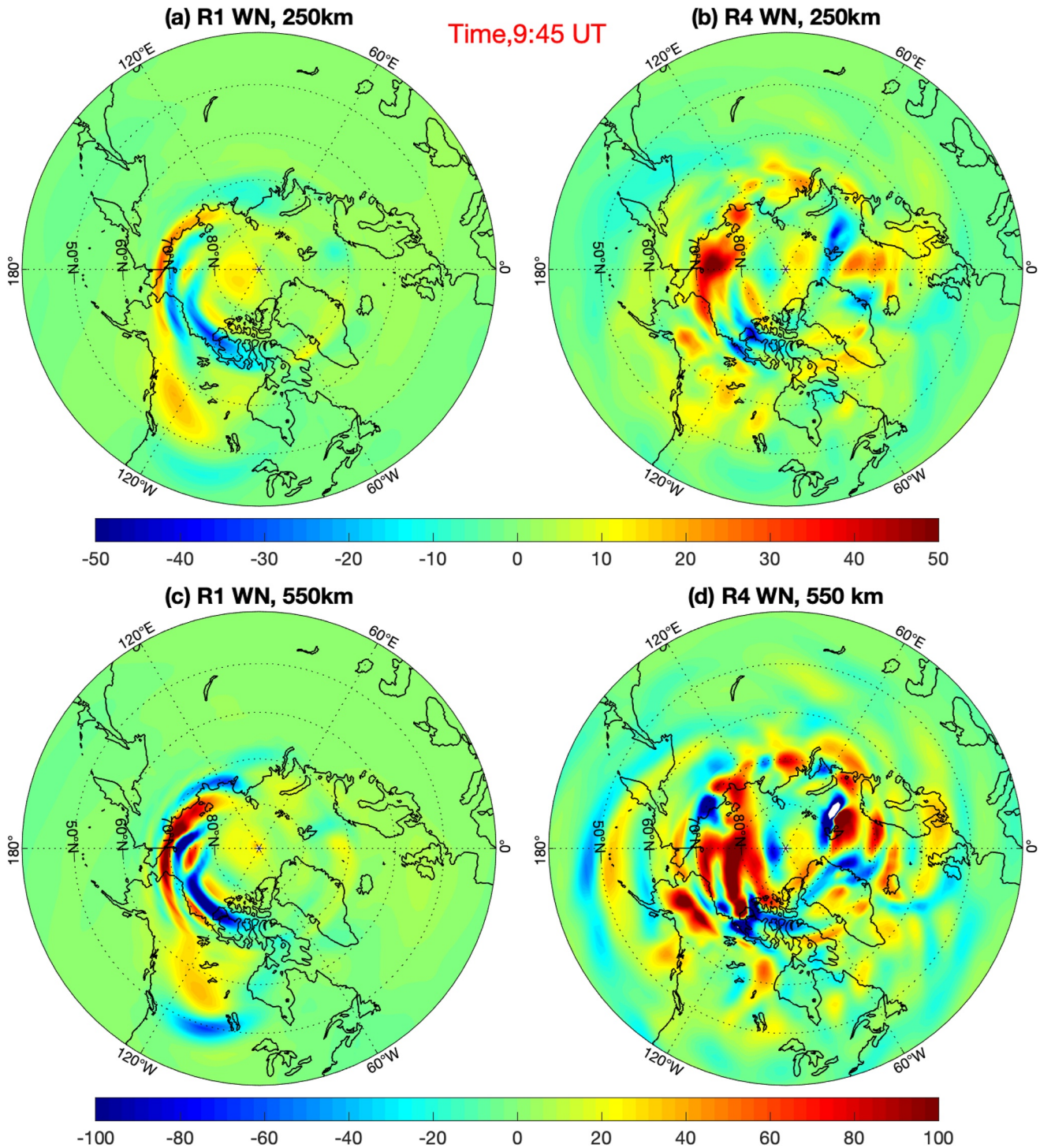

Figure 15. (a, b) Neutral vertical winds at ~250 km from R1 ($R_{a\_emp\_e\_emp}$) and R4 ($R_{a\_ assi\ \_e\_assi}$), respectively. (c, d) Are the same except at ~550 km. Unit is m/s.

to low latitudes likely due to the elevation of local heating and ion drag as a wave source; and (f) short-term temporal variability more comparable with the PFISR and FPI observations. In addition, the maximum values of Ne, Te, Ti, and Wn responses are better captured in assimilated model runs. The rms errors calculated from the differences between model results and observations decrease by 30%–50% compared to the default run. All these improvements show that the I-T responses to the St. Patrick's Day storm in reality have a larger dynamic range and more variability than those simulated by the default TIEGCM run with empirical driving conditions. Thus,

10.1029/2022SW003308

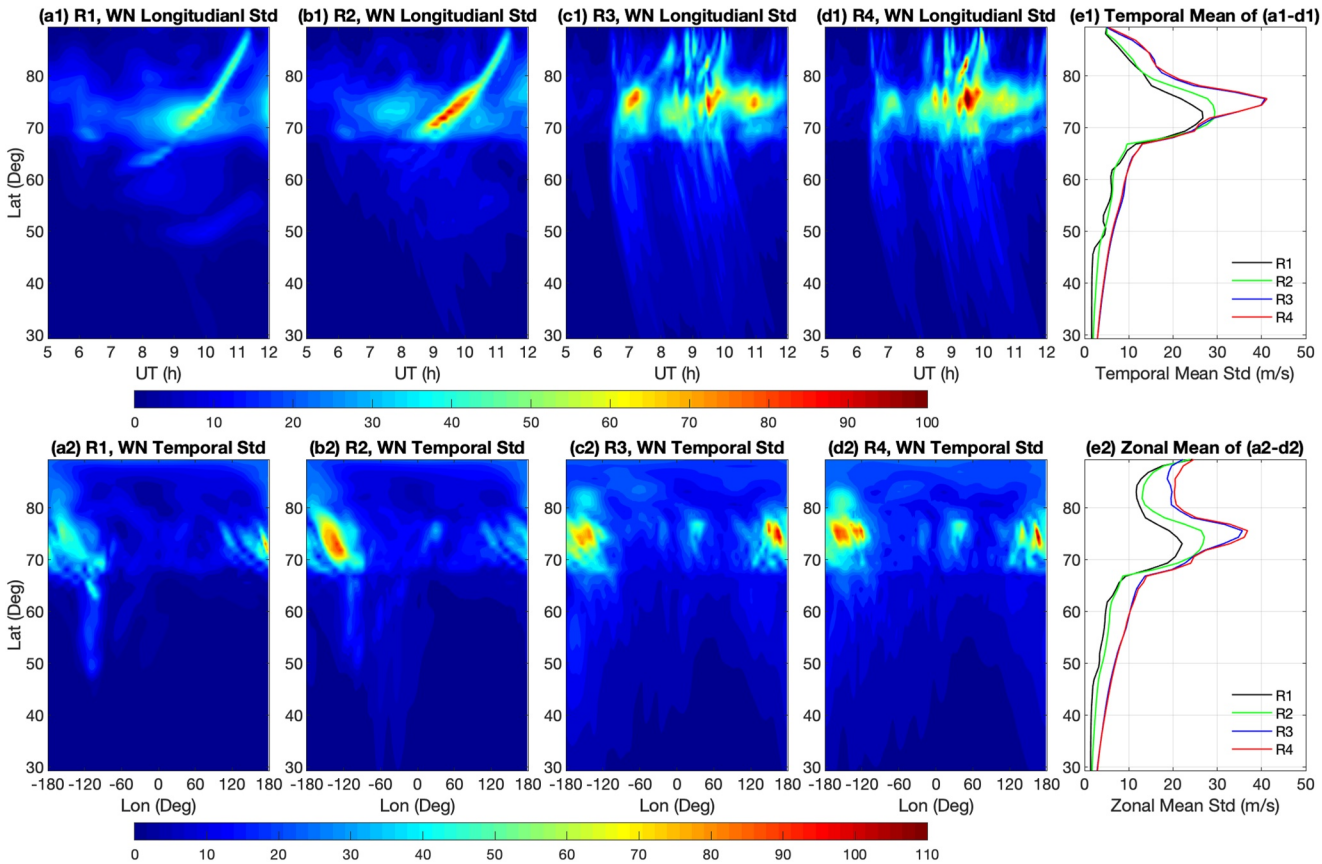

Figure 16. (a1–d1) Longitudinal variability (calculated as standard deviation along the longitude) of neutral vertical wind as a function of latitude and universal time at ~550 km. (e1) Temporal means of panels (a1–d1). (a2–d2) Temporal variability of neutral vertical wind as a function of latitude and longitude at ~550 km. (e2) Zonal (longitudinal) mean of panels (a2–d2). The unit is m/s.

we have shown that data assimilation of high-latitude drivers can help us better understand the storm impacts both locally and globally. Even though the data assimilation run is a significant improvement, the remaining discrepancies compared with observations include that the modeled TE is about ~1000 K colder than the PFISR observation in the F-region, which needs a further investigation.

Once the model drivers are refined with aurora and electric field data, and the outputs are systematically evaluated and found to be in better agreement with observations, this data-constrained model run is then used to diagnose the changes in the system responses, for which we use the longitudinal and temporal variability of neutral vertical winds as a proxy. Compared to the default run, the data assimilation run has shown stronger longitudinal (spatial) and temporal variabilities than the default run by a factor of 1.5–3. Since kinetic energy of wave is proportional to the square of wave perturbations, this would lead to an increase of kinetic energy received by the upper atmosphere by an order of magnitude. Such enhancement is not only seen in the auroral regions, but also prominent at middle and low latitudes, likely via the generation of TADs at high latitudes and then equatorward wave propagation. In addition, the refinement of high-latitude drivers can potentially change disturbance dynamo and penetration electric fields, which influence low-latitude and equatorial electrodynamics. Detailed analysis about the model performance at middle and low latitudes and comparison with observations there are worthwhile which deserves a future investigation.

Our work highlights the importance of observing the storm-time manifestation of magnetospheric drivers and I-T responses simultaneously in order to better understand neutral-ion coupling in the upper atmosphere, a prerequisite for the predictability of space weather. Such observations can also help constrain data assimilation models and evaluate their capabilities as well as limitations. The quality of data assimilation still highly depends on observations. Multi-point and simultaneous observations of ion drifts, auroral precipitation, electron densities,

and neutral responses such as density and wind, and temperature, such as those solicited by the Geospace Dynamics Constellation mission, are highly desirable.

Data Availability Statement

The code of Lattice Kriging for electric fields is published at https://github.com/hzfywhn/LatticeKriging. The data used to produce the figures are available at https://data.mendeley.com/datasets/km7g78b95b. The National Center for Atmospheric Research is sponsored by the National Science Foundation. The PFISR observations can be found at: https://data.amisr.com/database/61/experiment/20150317.001/.

Acknowledgments
We are grateful of the valuable discussion with Qiong Zhang, Whitney Huang, and Xiyan Tan at Clemson University concerning the data assimilation. We thank Donald Hampton and Mark Conde at University of Alaska Fairbanks for providing the FPI data. Xian Lu and Haonan Wu's work is supported by NASA Grants 80NSSC22K0018, NNX17AG10G, 80NSSC22K1010, 80NSSCK19K0810, and NSF Grants AGS-2149695, AGS-2012994, CAREER-1753214. Yukitoshi Nishimura's work is supported by NASA Grant 80NSSC18K0657, 80NSSC20K0604, 80NSSC20K0725, 80NSSC21K1321, and 80NSSC19K0546, NSF Grant AGS-1907698 and AGS-2100975, and AFOSR grant FA9559-16-1-0364. Wenbin Wang's work is supported in part by NASA Grants 80NSSC19K0080, 80NSSC20K0356, 80NSSC19K0835, 80NSSC20K0601 and NSF Grant AGS-2033843.

References

Codrescu, M. V., Fuller-Rowell, T. J., & Foster, J. C. (1995). On the importance of E-field variability for Joule heating in the high-latitude thermosphere. *Geophysical Research Letters*, *22*(17), 2393–2396. https://doi.org/10.1029/95GL01909

Cosgrove, R. B., & Codrescu, M. (2009). Electric field variability and model uncertainty: A classification of source terms in estimating the squared electric field from an electric field model. *Journal of Geophysical Research*, *114*(A6), A06301. https://doi.org/10.1029/2008JA013929

Cousins, E. D. P., Matsuo, T., & Richmond, A. D. (2013). Mesoscale and large-scale variability in high-latitude ionospheric convection: Dominant modes and spatial/temporal coherence. *Journal of Geophysical Research: Space Physics*, *118*(12), 7895–7904. https://doi.org/10.1002/2013JA019319

Cousins, E. D. P., & Shepherd, S. G. (2012a). Statistical characteristics of small-scale spatial and temporal electric field variability in the high-latitude ionosphere. *Journal of Geophysical Research*, *117*(A3), A03317. https://doi.org/10.1029/2011JA017383

Cousins, E. D. P., & Shepherd, S. G. (2012b). Statistical maps of small-scale electric field variability in the high-latitude ionosphere. *Journal of Geophysical Research*, *117*(A12), A12304. https://doi.org/10.1029/2012JA017929

Dang, T., Lei, J., Wang, W., Zhang, B., Burns, A., Le, H., et al. (2018). Global responses of the coupled thermosphere and ionosphere system to the August 2017 Great American Solar Eclipse. *Journal of Geophysical Research: Space Physics*, *123*(8), 7040–7050. https://doi.org/10.1029/2018JA025566

Dang, T., Zhang, B., Lei, J., Wang, W., Burns, A., Liu, H., et al. (2021). Azimuthal averaging–reconstruction filtering techniques for finite-difference general circulation models in spherical geometry. *Geoscientific Model Development*, *14*(2), 859–873. https://doi.org/10.5194/gmd-14-859-2021

Deng, Y., Huang, Y., Lei, J., Ridley, A. J., Lopez, R., & Thayer, J. (2011). Energy input into the upper atmosphere associated with high-speed solar wind streams in 2005. *Journal of Geophysical Research*, *116*(A5), A05303. https://doi.org/10.1029/2010JA016201

Fuller-Rowell, T. J., Rees, D., Quegan, S., Moffett, R. J., & Bailey, G. J. (1987). Interactions between neutral thermospheric composition and the polar ionosphere using a coupled ionosphere-thermosphere model. *Journal of Geophysical Research*, *92*(A7), 7744. https://doi.org/10.1029/JA092iA07p07744

Golovchanskaya, I. V., & Kozelov, B. V. (2010). On the origin of electric turbulence in the polar cap ionosphere. *Journal of Geophysical Research*, *115*(A9), A09321. https://doi.org/10.1029/2009JA014632

Hardy, D. A., Gussenhoven, M. S., & Holeman, E. (1985). A statistical model of auroral electron precipitation. *Journal of Geophysical Research*, *90*(A5), 4229. https://doi.org/10.1029/JA090iA05p04229

Heelis, R. A., Lowell, J. K., & Spiro, R. W. (1982). A model of the high-latitude ionospheric convection pattern. *Journal of Geophysical Research*, *87*(A8), 6339. https://doi.org/10.1029/JA087iA08p06339

Heinselman, C. J., & Nicolls, M. J. (2008). A Bayesian approach to electric field and E-region neutral wind estimation with the Poker Flat advanced modular incoherent scatter radar. *Radio Science*, *43*(5), RS5013. https://doi.org/10.1029/2007RS003805

Heppner, J. P., Liebrecht, M. C., Maynard, N. C., & Pfaff, R. F. (1993). High-latitude distributions of plasma waves and spatial irregularities from DE 2 alternating current electric field observations. *Journal of Geophysical Research*, *98*(A2), 1629–1652. https://doi.org/10.1029/92JA01836

Huang, C. Y., & Burke, W. J. (2004). Transient sheets of field-aligned current observed by DMSP during the main phase of a magnetic superstorm. *Journal of Geophysical Research*, *109*(A6), A06303. https://doi.org/10.1029/2003JA010067

Huang, Y., Wu, Q., Huang, C. Y., & Su, Y.-J. (2016). Thermosphere variation at different altitudes over the northern polar cap during magnetic storms. *Journal of Atmospheric and Solar-Terrestrial Physics*, *146*, 140–148. https://doi.org/10.1016/j.jastp.2016.06.003

Knipp, D., Eriksson, S., Kilcommons, L., Crowley, G., Lei, J., Hairston, M., & Drake, K. (2011). Extreme Poynting flux in the dayside thermosphere: Examples and statistics. *Geophysical Research Letters*, *38*(16), L16102. https://doi.org/10.1029/2011GL048302

Knipp, D. J., Tobiska, W. K., & Emery, B. A. (2004). Direct and indirect thermospheric heating sources for solar cycles 21–23. *Solar Physics*, *224*(1), 495–505. https://doi.org/10.1007/s11207-005-6393-4

Kozelov, B. V., & Golovchanskaya, I. V. (2006). Scaling of electric field fluctuations associated with the aurora during northward IMF. *Geophysical Research Letters*, *33*(20), L20109. https://doi.org/10.1029/2006GL027798

Larsen, M. F., & Meriwether, J. W. (2012). Vertical winds in the thermosphere. *Journal of Geophysical Research*, *117*(A9), A09319. https://doi.org/10.1029/2012JA017843

Lu, G., Baker, D. N., McPherron, R. L., Farrugia, C. J., Lummerzheim, D., Ruohoniemi, J. M., et al. (1998). Global energy deposition during the January 1997 magnetic cloud event. *Journal of Geophysical Research*, *103*(A6), 11685–11694. https://doi.org/10.1029/98JA00897

Lu, G., Richmond, A. D., Emery, B. A., & Roble, R. G. (1995). Magnetosphere–ionosphere–thermosphere coupling: Effect of neutral winds on energy transfer and field-aligned current. *Journal of Geophysical Research*, *100*(A10), 19643–19659. https://doi.org/10.1029/95ja00766

Lu, X., Chen, C., Huang, W., Smith, J. A., Chu, X., Yuan, T., et al. (2015). A coordinated study of 1h mesoscale gravity waves propagating from Logan to Boulder with CRRL Na Doppler lidars and temperature mapper. *Journal of Geophysical Research: Atmospheres*, *120*(19), 10006–10021. https://doi.org/10.1002/2015JD023604

Lu, X., Chu, X., Li, H., Chen, C., Smith, J., & Vadas, S. (2017). Statistical characterization of high-to-medium frequency mesoscale gravity waves by lidar-measured vertical winds and temperatures in the MLT. *Journal of Atmospheric and Solar-Terrestrial Physics*, *162*, 3–15. https://doi.org/10.1016/j.jastp.2016.10.009

Mende, S. B., Harris, S. E., Frey, H. U., Angelopoulos, V., Russell, C. T., Donovan, E., et al. (2008). The THEMIS array of ground-based observatories for the study of auroral substorms. *Space Science Reviews*, *141*(1–4), 357–387. https://doi.org/10.1007/s11214-008-9380

Newell, P. T., Sotirelis, T., & Wing, S. (2009). Diffuse, monoenergetic, and broadband aurora: The global precipitation budget. *Journal of Geophysical Research*, *114*(A9), A09207. https://doi.org/10.1029/2009JA014326

Nishimura, Y., Deng, Y., Lyons, L. R., McGranaghan, R. M., & Zettergren, M. D. (2021). Multiscale dynamics in the high-latitude ionosphere. In *Ionosphere dynamics and applications*, (pp. 49–65). https://doi.org/10.1002/9781119815617.ch3

Nishimura, Y., & Lyons, L. (2021). The active magnetosphere: Substorms and storms, magnetospheres in the solar system (pp. 277–291).

Nishimura, Y., Verkhoglyadova, O., Deng, Y., & Zhang, S. R. (2021). *Cross-scale coupling and energy transfer in the magnetosphere-ionosphere-thermosphere system* (Vol. 1–63). Elsevier.

Paxton, L. J., & Meng, C.-I. (1999). Auroral imaging and space-based optical remote sensing. *Johns Hopkins APL Technical Digest*, *20*, 556.

Paxton, L. J., Morrison, D., Zhang, Y., Kil, H., Wolven, B., Ogorzalek, B. S., et al. (2002). Validation of remote sensing products produced by the special sensor ultraviolet scanning imager (SSUSI): A far UV-imaging spectrograph on DMSP F-16. In *Proceeding of society of photo-optical instrumentation engineers* (Vol. 4485). https://doi.org/10.1117/12.454268

Qian, L., Burns, A. G., Emery, B. A., Foster, B., Lu, G., Maute, A., et al. (2014). The NCAR TIE-GCM: A community model of the coupled thermosphere/ionosphere system. *Geophysical Monograph Series*, 73–83. https://doi.org/10.1002/9781118704417.ch7

Richmond, A. D., Ridley, E. C., & Roble, R. G. (1992). A thermosphere/ionosphere general circulation model with coupled electrodynamics. *Geophysical Research Letters*, *19*(6), 601–604. https://doi.org/10.1029/92GL00401

Richmond, A. D., & Thayer, J. P. (2000). Ionospheric electrodynamics: A tutorial. *Magnetospheric Current Systems*, 131–146. https://doi.org/10.1029/GM118p0131

Roble, R. G., & Ridley, E. C. (1987). An auroral model for the NCAR thermospheric general circulation model (TGCM). In *Annales Geophysicae - Series A: Upper atmosphere and space sciences*, (Vol. 5, No. (6), pp. 369–382). Retrieved from http://n2t.net/ark:/85065/d70v8ckz

Sheng, C., Deng, Y., Zhang, S.-R., Nishimura, Y., & Lyons, L. R. (2020). Relative contributions of ion convection and particle precipitation to exciting large-scale traveling atmospheric and ionospheric disturbances. *Journal of Geophysical Research: Space Physics*, *125*(2), e2019JA027342. https://doi.org/10.1029/2019JA027342

Thayer, J. P., & Semeter, J. (2004). The convergence of magnetospheric energy flux in the polar atmosphere. *Journal of Atmospheric and Solar-Terrestrial Physics*, *66*(10), 807–824. https://doi.org/10.1016/j.jastp.2004.01.035

Thayer, J. P., Vickrey, J. F., Heelis, R. A., & Gary, J. B. (1995). Interpretation and modeling of the high-latitude electromagnetic energy flux. *Journal of Geophysical Research*, *100*(A10), 19715. https://doi.org/10.1029/95JA01159

Vadas, S. L. (2013). Compressible f-plane solutions to body forces, heatings, and coolings, and application to the primary and secondary gravity waves generated by a deep convective plume. *Journal of Geophysical Research: Space Physics*, *118*(5), 2377–2397. https://doi.org/10.1002/jgra.50163

Wang, W., Burns, A. G., Solomon, S., & Killeen, T. L. (2005). High-resolution, coupled thermosphere-ionosphere models for space weather applications. *Advances in Space Research*, *36*(12), 2486–2491. https://doi.org/10.1016/j.asr.2003.11.025

Weimer, D. R. (2005). Improved ionospheric electrodynamic models and application to calculating Joule heating rates. *Journal of Geophysical Research*, *110*(A5), A05306. https://doi.org/10.1029/2004JA010884

Wu, H., & Lu, X. (2022). Data assimilation of high-latitude electric fields: Extension of a multi-resolution Gaussian process model (Lattice Kriging) to vector fields. *Space Weather*, *20*(1), e2021SW002880. https://doi.org/10.1029/2021SW002880

Wu, H., Lu, X., Lu, G., Chu, X., Wang, W., Yu, Z., et al. (2020). Importance of regional-scale auroral precipitation and electrical field variability to the storm-time thermospheric temperature enhancement and inversion layer (TTEIL) in the Antarctic E region. *Journal of Geophysical Research: Space Physics*, *125*(9), e2020JA028224. https://doi.org/10.1029/2020JA028224

Wu, H., Tan, X., Zhang, Q., Huang, W., Lu, X., Nishimura, Y., & Zhang, Y. (2022). Multiresolution data assimilation for auroral energy flux and mean energy using DMSP SSUSI, THEMIS ASI, and an empirical model. *Space Weather*, *20*(9), e2022SW003146. https://doi.org/10.1029/2022SW003146

Zhang, S.-R., Erickson, P. J., Zhang, Y., Wang, W., Huang, C., Coster, A. J., et al. (2017). Observations of ion-neutral coupling associated with strong electrodynamic disturbances during the 2015 St. Patrick's Day storm. *Journal of Geophysical Research: Space Physics*, *122*(1), 1314–1337. https://doi.org/10.1002/2016JA023307

Zhang, Y., & Paxton, L. J. (2008). An empirical Kp-dependent global auroral model based on TIMED/GUVI FUV data. *Journal of Atmospheric and Solar-Terrestrial Physics*, *70*(8–9), 1231–1242. https://doi.org/10.1016/j.jastp.2008.03.008